https://doi.org/10.5194/egusphere-2026-6450
Preprint. Discussion started: 3 November 2026
© Author(s) 2026. CC BY 4.0 License.

Eulerian space-time statistics of rotational motions from drifters using Gaussian processes

William C Edge[1,2], Matt D Rayson[1,2], Nicole L Jones[1,2], and Lachlan C Astfalck[3]

[1]The School of Earth and Oceans, The University of Western Australia, Australia
[2]The Oceans Institute, The University of Western Australia, Australia
[3]The School of Mathematics and Statistics, The University of New South Wales, Australia

Correspondence: William C Edge (william.edge@uwa.edu.au)

Abstract.

We applied a Gaussian process regression framework to horizontal velocity data from ocean drifters to infer the space-time scales and total energy of rotational motions in contrasting shelf and ocean regions. A space-time covariance kernel function was chosen to represent rotational motions and its characteristic parameters were inferred directly from the data. We applied the framework to contrasting ocean and shelf environments and found consistent spatial anisotropy in the length scales of each velocity component in both regions, a feature of rotational motion dynamics. The framework resolved rotational features in a macro-tidal shelf environment beyond the limits of nadir altimetry, including a feature with a Rossby number $\approx$1. The framework estimated time scales in both regions to be less than 10 days, driven by a mix of temporal evolution and low frequency advection. We demonstrate the feasibility of spatiotemporal inference from sparse unstructured oceanographic observations, an approach made tractable using Vecchia's approximation to a Gaussian process, which shows potential for inference studies on large and multi-platform datasets.

https://doi.org/10.5194/egusphere-2026-6450
Preprint. Discussion started: 3 November 2026
© Author(s) 2026. CC BY 4.0 License.

1 Introduction

Mesoscale and submesoscale motions dominate observations of near-surface kinetic energy (Ferrari and Wunsch, 2009; Chelton et al., 2011). These primarily *rotational motions* are inherently spatiotemporal, captured by numerical models as a diffuse cusp of energy in frequency-wavenumber spectral space spread along the nondispersive line (see Arbic et al., 2014; Qiu et al., 2018; Torres et al., 2018). Obtaining equivalent multi-dimensional information from in-situ sources is challenging as observations only provide a narrow window into the behaviour of these flow fields. Motivated by modelling studies and recent spatiotemporal inference on synthetic data (Ponte et al., 2024), here we present and evaluate a framework to estimate the joint spatiotemporal covariance structure and corresponding power spectrum of rotational motions directly from surface drifter observations in two exemplar regions of the ocean.

Previous characterisations have focused on recovering spatial structure while divesting temporal structure, or vice versa. Structure functions or wavenumber power spectra provide scale-dependent information on rotational motions, but are limited to space only (Bühler et al., 2014; Wang, 2021). Mooring pairs can be used to estimate time scales of rotational motions for fixed separation distances (Callies et al., 2020). Satellite altimetry and mixed satellite - in-situ approaches provide a synoptic spatiotemporal view of motions at larger scales (Stammer, 1998; Ubelmann et al., 2021; Chiswell et al., 2007), but miss smaller features, including most shelf-sea motions.

Drifters occupy an observational niche for characterising the spatiotemporal structure of rotational motions because they resolve lateral and temporal differences at high resolution for extended periods. Drifters experience the integrated force of all processes that contribute to ocean surface currents and thus contain a detailed spatiotemporal record. Lagrangian spectra blur spatial and temporal features together (Caspar-Cohen et al., 2022), complicating their disentanglement. The primary hurdles to unlocking the detailed spatiotemporal information of drifter data are their extreme sparsity (even when considering large clusters) and their highly irregular paths. These features can prohibit the extension of existing approaches, such as structure functions, to the higher dimensions required for spatiotemporal analysis.

In this work we use a Gaussian process (GP) regression framework (Moss et al., 2026) to first separate low frequency flows from rotational motions and then to characterise the rotational motions themselves. This requires the implementation of a multi-scale analysis method for the decomposition, after which the rotational motions are represented by a zero-mean GP from which we can infer the energy and space and time length scales. We show how this framework can approximately extract and interpolate rotational currents from drifter records in contrasting open ocean and macro-tidal shelf regions, even under low signal-to-noise conditions. The inferred space and time length scales highlight the different dynamics in each region.

2 Spatiotemporal covariance, spectra, and their relation to Gaussian processes

Ocean variables can be statistically represented by their multi-dimensional power spectral density (herein PSD, e.g., Wortham and Wunsch, 2014), or its Fourier pair, the auto-covariance (herein ACF), both a representation of the variable's second-order statistics. Attempts to estimate the empirical 3D (x, y, t) frequency-wavenumber PSD of rotational surface currents have generally been limited to satellite altimetry and numerical studies. Wunsch and Stammer (1995) used satellite altimetry to

https://doi.org/10.5194/egusphere-2026-6450
Preprint. Discussion started: 3 November 2026
© Author(s) 2026. CC BY 4.0 License.

compute the 3D PSD of sea surface height, but instrument and orbit path constraints prohibited temporal resolution below ~ 50 km and $\sim$10 days (geostationary satellites can resolve higher temporal frequencies but are limited to optical and infrared image-derived quantities). Numerical simulations have provided insight into the spatiotemporal structure of rotational currents (Arbic et al., 2014; Qiu et al., 2018; Torres et al., 2018) using gridded model output, but these results require observation-based validation. Wortham and Wunsch (2014) synthesised a broad range of observations to obtain a global frequency-wavenumber spectral model for balanced motions. While they provided a useful picture, observations at scales less than 100 km were limited and sometimes inconsistent. This constraint and the clear regional variability suggest more work is needed to confirm the spatiotemporal characteristics of rotational motions.

Covariance methods can fill this gap, allowing for empirical and modelled analysis methods with unstructured observations. The most common approach in oceanography is the second-order structure function (inverse ACF), which provides a scale-dependent empirical decorrelation estimate (e.g., Balwada et al., 2016; Callies et al., 2020; Wang, 2021). Structure functions have known limitations. At smaller lags structure functions are biased by the vorticity and divergence properties of larger scale motions (Pearson et al., 2020). At large lags structure function estimates are unreliable (Cressie, 1985), a problem that compounds in higher dimensional settings. To overcome these limitations we model the ACF using GP regression. This modelled covariance approach is recommended over structure functions in higher dimensions because it does not require arbitrary binning of lags, the error in the estimate of the ACF does not grow at large lags, and it provides a robust framework for uncertainty quantification. This approach comes at the expense of empirical flexibility, with the decorrelation behaviour forced by a chosen model's shape. The ability to move between spectral and covariance space with the Fourier transform provides useful comparisons between the different approaches.

GP regression is a covariance modelling framework frequently used in oceanographic literature (Berlinghieri et al., 2023; Elipot et al., 2016; Ponte et al., 2024; Aravind et al., 2025), often under different names and in varying forms (Wunsch, 1996; Le Traon, 1990; Ubelmann et al., 2022; Gray and Riser, 2015). We can treat an ocean parameter as a random field that is completely specified by its mean function (first moment, μ) and covariance kernel (second moment, Σ), where the covariance kernel encapsulates the statistical properties of the residual component. Formally, let $\eta(\cdot)$ denote such a field over a spatio-temporal domain $\mathcal{D}$, with mean function $\mu(\mathbf{z})$ and covariance kernel $c(\mathbf{z}, \mathbf{z}')$ for $\mathbf{z}, \mathbf{z}' \in \mathcal{D}$. The defining feature of a GP is that the values it takes at any finite set of locations are jointly multivariate normal. The field is never observed everywhere, only at the finite number of locations at which measurements are made, so it is this finite-dimensional distribution that we work with in practice. Write $\mathbf{y} = \{\eta(\mathbf{z}_1), \ldots, \eta(\mathbf{z}_n)\}^\top$ for the field evaluated at the observation locations $\mathbf{z}_1, \ldots, \mathbf{z}_n$, the mean vector has entries $\mu_i = \mu(\mathbf{z}_i)$ and the covariance matrix has entries $\Sigma_{ij} = C(\mathbf{z}_i, \mathbf{z}_j)$, giving

$$\mathbf{y} \sim \mathcal{N}(\mu, \Sigma). \tag{1}$$

The kernel supplies the covariance matrix for whatever configuration of locations the data happen to have, however irregular. Further, as the same kernel governs any enlarged set of locations, it also supplies the joint distribution of the observations with the field at unobserved points, which is what allows the process to be interpolated away from the measurements. The GP framework allows for a wide array of valid covariance functions, which govern the second order structure of the process.

https://doi.org/10.5194/egusphere-2026-6450
Preprint. Discussion started: 3 November 2026
© Author(s) 2026. CC BY 4.0 License.

This enables the wealth of oceanographic spectral analysis research to inform covariance model selection (Wortham and Wunsch, 2014; Rayson et al., 2025; Zheng et al., 2026). In addition, the framework is second-order consistent for non-Gaussian distributed data, assuming the covariance function is correctly specified. This means that we can still estimate the second-order properties, such as length scales, with departures from Gaussianity (Guyon, 1982; Astfalck, 2026). Taken together, these features make GP regression highly flexible and well-suited to many oceanographic applications.

The GP framework has two key applications which are useful for oceanography applications, inference and prediction. GP inference can be used to find the optimal fit of a chosen covariance model given some observations, i.e., an inferred statistical characterisation. By maximising the likelihood we find the best form of Σ to represent our observations (Rasmussen and Williams, 2006), thus fitting an optimal set of model parameters to represent the process' second-order statistics (with respect to our model choice). Here we perform the optimisation in a Bayesian framework which allows us to constrain the inference of parameters in θ to physically plausible values. We performed the optimisation with both standard (single point) maximum a posteriori (MAP) and Markov-Chain Monte Carlo (MCMC), which provides a full posterior distribution of the joint parameter set [Appendix D]. GP predictions can be used to interpolate between observations or forecast with quantified uncertainty. Predictions far from observations will tend back towards μ and uncertainty will grow to the process variance.

Previous use of a GP for multi-dimensional dataset inference is limited because of the computational burden (e.g. Aravind et al., 2025; Xia et al., 2025). Here we use a recently developed method in statistical literature to accommodate larger datasets. Vecchia's approximation to a Gaussian process (Vecchia, 1988; Katzfuss and Guinness, 2021) approximates a full GP density as the product of many small conditional distributions. By sub-setting the full n observations of each conditional distribution to a small number of neighbours, n_v, computation is reduced from $\mathcal{O}(n^3)$ computation into many small $\mathcal{O}(n_v^3)$ computations, with costs now scaling by $\mathcal{O}(n \cdot n_v^3)$. An extended description is presented in Appendix A.

3 Data & Methods

3.1 Site & Drifters

We used a dataset of 122 drifters released in the Browse Basin region as part of a targeted academic–industry campaign between May 2020 and September 2023 [Figure 1] (Siji and Pattiaratchi, 2025). The Browse Basin, representing our *shelf* region [Figure 1], is a macro-tidal site influenced by both a shelf break and coral atoll bathymetry. The basin is primarily forced by strong semidiurnal tides and seasonal trade winds. Strong internal tides have been observed in satellite imagery and mooring records (Rayson et al., 2011; Gong et al., 2021). Observed low frequency seasonal currents are driven by wind-forced Kelvin waves and the nearby Indonesian-Through-Flow (ITF, Ridgway and Godfrey, 2015).

The majority of the Browse Basin drifters dispersed along-shelf in both directions before travelling westward upon leaving the shelf. Most (96) moved into our chosen *ocean* analysis region in the South-eastern Indian ocean [Figure 1]. The *ocean* region is dominated by the seasonal ITF current which transports material westward outside of the Austral summer (Gordon, 1986). The region is a hotspot of mesoscale eddy activity (Siji and Pattiaratchi, 2025) and semidiurnal internal tides generated near Indonesia and Australia propagate through the region in multiple directions (Gong et al., 2021).

https://doi.org/10.5194/egusphere-2026-6450
Preprint. Discussion started: 3 November 2026
© Author(s) 2026. CC BY 4.0 License.

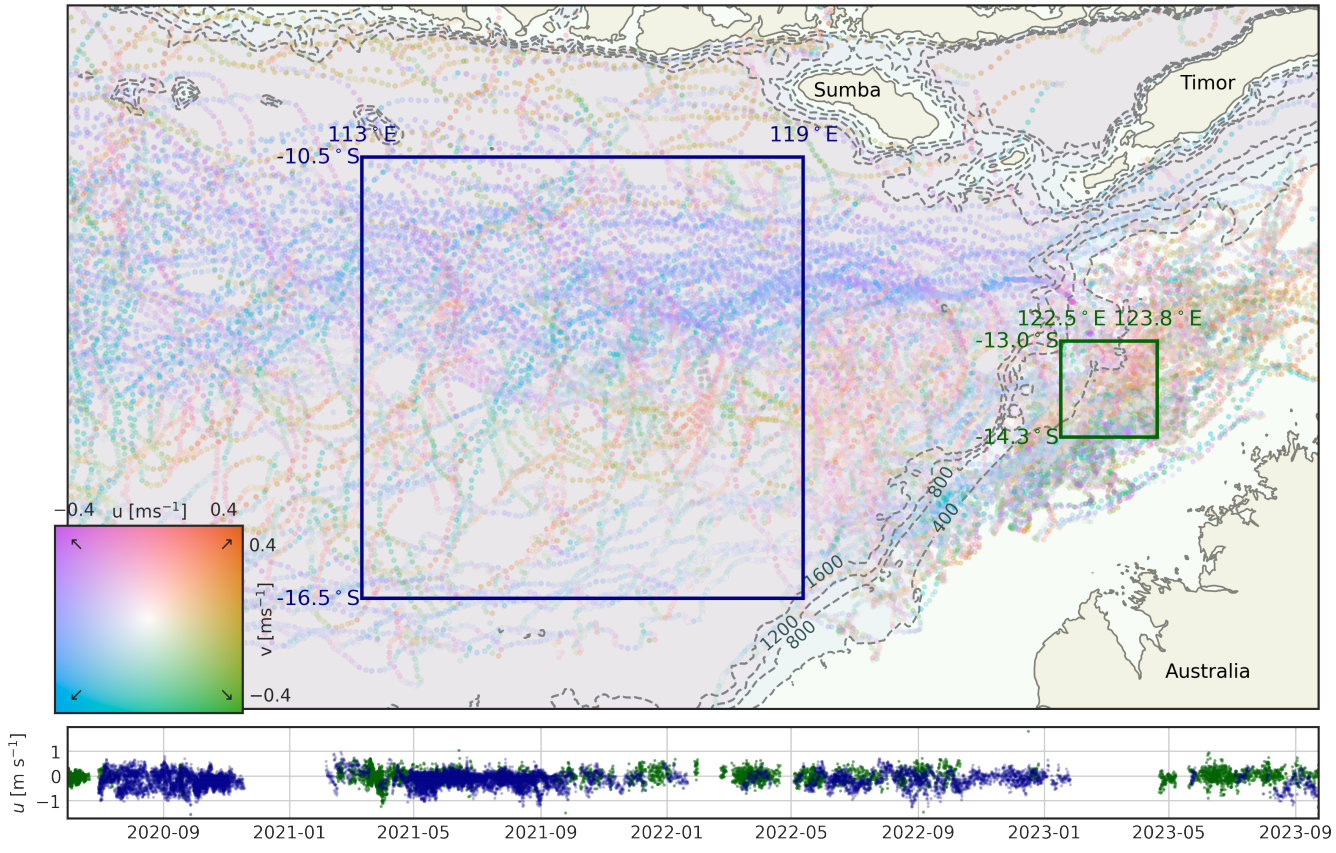


Figure 1. All drifter data used in this work spanning from May 2020 to September 2023, shown on the map as coloured points representing the east-west (u) and north-south (v) components of horizontal velocity (colour map bottom right). The *shelf* region is the *green* box and the *ocean* region is the *blue* box. Time series of *shelf* (*green*) and *ocean* (*blue*) u velocity shown below.

Most of the drifters (111) were undrogued and designed to float with minimal protrusion above the surface to limit wind-drag on the device (van der Mheen et al., 2020; Siji and Pattiaratchi, 2025). The final eleven (11) were Carthe drifters with a 0.4 m drogue. Drifters sampled at approximately 5 minute intervals and could miss an upload time (sometimes missing many uploads) so the resulting dataset was irregular (unstructured) in both time and space. Drifter data was quality controlled [Appendix B] and the subsequent good data was subsampled (not interpolated) to the observation nearest to a 6-hour time step. The resulting datasets, n =6273 and n =14586 for the *shelf* and *ocean* respectively, were used without any filtering or other modifications [Figure 1].

3.1.1 Other data

To facilitate the comparison of surface current variability we extracted 30 years of eddy-resolving numerical Bluelink reanalysis (BRAN) output (Chamberlain et al., 2021). Estimates of wind-driven Ekman-balanced currents at the surface were obtained

https://doi.org/10.5194/egusphere-2026-6450
Preprint. Discussion started: 3 November 2026
© Author(s) 2026. CC BY 4.0 License.

from Copernicus-Globcurrent at 1-hour intervals over the two regions of interest (Rio et al., 2014). These model outputs were linearly interpolated to drifter coordinates.

3.2 Decomposition approach

To characterise rotational motions (our small-scale process in a multi-scale analysis framework) we need to remove the large-scale (seasonal) and unresolved-scale (tidal frequency) processes. We hypothesise that our observed ocean currents at both seasonal and rotational scales can be described by the first and second moments of a Gaussian process (equation 1), respectively (see Zang and Wunsch, 2001). The seasonal currents, $\overline{\mathbf{u}}$, were represented by annual and semi-annual harmonics [detailed in Appendix C]. The rotational currents, $\mathbf{u}'$, were represented by the small-scale covariance kernel, C. Higher frequency motions, u_ϵ, like tides and internal waves, were treated as an unresolved white noise process inside C but could be represented by their own covariance model. In addition, we removed Ekman-balanced currents, $\mathbf{u}_{Ek}$, obtained from Globcurrent. Thus our observations are represented by the Gaussian process,

$$\mathbf{y}(z) \sim \mathcal{GP}\left(\overline{\mathbf{u}}(z), C(\theta)\right) \quad \text{where} \quad \mathbf{y} = \overline{\mathbf{u}} + \mathbf{u}_{Ek} + \mathbf{u}' + u_\epsilon. \tag{2}$$

Here the covariance model C has parameters θ (used to compute the associated covariance matrix $\Sigma_{\mathbf{R}}$). This model was chosen to target the frequency-wavenumber PSD region containing the continuum of rotational motions, noting that a westward propagation component, which centres spectral energy along the nondispersive line, was not included in this work so we do not expect to fully capture the high wavenumber component of the wavenumber-frequency cusp. We distinguish raw observations, $\mathbf{y}$, from decomposition outputs, $\mathbf{u}$, where both represent the bivariate horizontal velocity vector field u, v (eastward and northward velocity).

To estimate and remove the seasonal currents we used the GP formulation with a parametric mean function (Wunsch, 1996). We used this over generalised least squares because it can include an *a priori* covariance matrix, $\Sigma_{\mathbf{B}}$, to constrain the parameter coefficients. This was critical for our dataset where the large-scale field was insufficiently observed and employing least squares risked over-fitting the large-scale component. Thus, together with C, equation 2 can be re-written as

$$\mathbf{y} = \mathbf{H}\mathbf{x} + g(z) + \mathbf{u}_{Ek}, \qquad \text{where} \qquad g(z) \sim \mathcal{GP}(0, C(\theta)) \qquad \text{and} \qquad \mathbf{x} \sim \mathcal{N}(0, \Sigma_{\mathbf{B}}), \tag{3}$$

with z the coordinate in horizontal space and time (x, y, t). Here $\mathbf{H}$ is the seasonal harmonic model, $\mathbf{x}$ are the inferred model coefficients, and $g(z)$ is the rotational motion GP.

Using the GP formulation we computed the *maximum a posteriori* (MAP) seasonal current parameters $\mathbb{E}[\mathbf{x}|\mathbf{y}]$, i.e., the posterior estimate of $\mathbf{x}$, as

$$\mathbb{E}[\mathbf{x}|\mathbf{y}] = \Sigma_{\mathbf{B}}\mathbf{H}^{\mathsf{T}}\left(\mathbf{H}\Sigma_{\mathbf{B}}\mathbf{H}^{\mathsf{T}} + \Sigma_{\mathbf{R}}\right)^{-1}\mathbf{y}. \tag{4}$$

We computed the uncertainty of the seasonal currents from the posterior error covariance of the parameters, $\mathbb{V}[\mathbf{x}]$, as

$$\mathbb{V}[\mathbf{x}] = \Sigma_{\mathbf{B}} - \Sigma_{\mathbf{B}}\mathbf{H}^{\mathsf{T}}\left(\mathbf{H}\Sigma_{\mathbf{B}}\mathbf{H}^{\mathsf{T}} + \Sigma_{\mathbf{R}}\right)^{-1}\mathbf{H}\Sigma_{\mathbf{B}}. \tag{5}$$

https://doi.org/10.5194/egusphere-2026-6450
Preprint. Discussion started: 3 November 2026
© Author(s) 2026. CC BY 4.0 License.

In equations 4 and 5, $\Sigma_{\mathbf{B}}$ is the *a priori* covariance matrix, computed from a covariance function and used to constrain the spatial distribution of $\mathbf{x}$. It is distinct from the rotational motion covariance matrix, $\Sigma_{\mathbf{R}}$. For this study, $\Sigma_{\mathbf{B}}$ was computed as the Kronecker product of the *a priori* variance of low frequency motions with a $n \times n$ spatial Matérn covariance model using fixed (not inferred) parameters [see Table 1 for details].

The seasonal currents were computed as $\mathbb{E}[\mathbf{x}|\mathbf{y}]$ and subtracted from the observations. This altered our treatment of seasonal currents from stochastic to deterministic. As a result, uncertainty (in $\mathbb{V}[\mathbf{x}]$) was not propagated into the inference on rotational motions. Uncertainty in the rotational current predictions due to the uncertainty in the seasonal current predictions can still be computed from the cross-covariance of the error terms but is not shown here. We note that we preferred the data-driven decomposition approach presented here, but any suitable method of low frequency current estimation, including using a hind cast numerical model, would likely be sufficient to remove low frequency motions before characterising the rotational motions.

3.3 The statistical characterisation of rotational motions

Our covariance model represents the spatiotemporal behaviour of rotational motions. We chose to use Matérn covariance functions which have linear spectral slopes in log-log space. The vector of covariance model parameters, θ, contains the process energy, σ^2, the unresolved energy ϵ^2 (noise), and the 3D anisotropic length scales, L_x, L_y, L_t. The length scale parameters are the characteristic decorrelation distance of the covariance function. The inferred (most likely) parameter set, with respect to our observations and covariance model choice, was used to predict rotational currents from any point in time and space to any other point in time and space, i.e., $\mathbb{R}^3 \rightarrow \mathbb{R}$, with quantified uncertainty.

To represent the rotational currents we fixed the Matérn parameter ν to 3/2 for the *shelf* and 1/2 for the *ocean*, fixing the spectral slopes in all three dimensions to -4 and -2, respectively. Wortham and Wunsch (2014) modelled the mesoscale oceanic variability spectrum and found a spectral slope of -2 (ν=1/2) best represented horizontal velocity in the open ocean (with ν=1/2 the Matérn is equal to an exponential function). Inference in the *shelf* region using ν=1/2 would not converge, so instead ν=3/2 was used. The implications of this choice are discussed later (Section 5.3). The n-dimensional form of the selected Matérn 1/2 and Matérn 3/2 functions are

$$C^{1/2}(\theta) = \sigma^2 \exp(-d) \qquad \text{and} \qquad C^{3/2}(\theta) = \sigma^2(1+\sqrt{3}d)\exp(-\sqrt{3}d), \tag{6}$$

respectively, where σ is the standard deviation of rotational currents and d is the scaled distance between two points z and z', computed in 3D as

$$d = ||\mathbf{L}^{-1}(z - z')||, \qquad \text{where} \qquad \mathbf{L} = \text{diag}(L_x, L_y, L_t). \tag{7}$$

We also tested 3D rotation of the covariance function using an additional three parameters, but they did not improve the inference and were not included.

The unresolved processes, u_ϵ, were represented as independent and identically distributed (i.i.d.) error, $\epsilon_{i.i.d.}$, (white noise) and were expected to contain significant barotropic and baroclinic tidal energy, based on our covariance model and choice to subsample to ~6 hours. The full parameter set to be inferred was thus $\theta = [\sigma, L_x, L_y, L_t, \epsilon_{i.i.d.}]$. Prior distributions for

https://doi.org/10.5194/egusphere-2026-6450
Preprint. Discussion started: 3 November 2026
© Author(s) 2026. CC BY 4.0 License.

Table 1. Hyper-parameters for multi-scale analysis. Where two values are separated by a semicolon they indicate the *shelf* and then *ocean* values.

Matérn parameter	$\Sigma_{\mathbf{B}}$ hyper-parameters (fixed)	C priors
σ [m s^{-1}]	0.05; 0.1	$\lvert\mathcal{N}(0, 0.1)\rvert$
ν	3/2	3/2; 1/2 (fixed)
L_x [km]	75; 150	$\lvert\mathcal{N}(0, 40)\rvert$; $\lvert\mathcal{N}(0, 100)\rvert$
L_y [km]	75; 150	$\lvert\mathcal{N}(0, 40)\rvert$; $\lvert\mathcal{N}(0, 100)\rvert$
L_t [days]	-	$\ln\mathcal{N}(1.95, 0.35)$
$\epsilon_{i.i.d.}$ [m s^{-1}]	-	$\ln\mathcal{N}(-2.12, 0.4)$

Bayesian optimisation (see Section 3.4) were supplied for all parameters [Table 1]. Finally, the Matérn covariance functions have analytical forms for the corresponding PSD, which in 3D are

$$S_{1/2}(\mathbf{k}) = \frac{8\pi\sigma^2 \cdot \det(\mathbf{L})}{\left(1 + 4\pi^2 ||\mathbf{Lk}||^2\right)^2} \quad \text{and} \quad S_{3/2}(\mathbf{k}) = \frac{96\sqrt{3}\pi\sigma^2 \cdot \det(\mathbf{L})}{\left(3 + 4\pi^2 ||\mathbf{Lk}||^2\right)^3}, \tag{8}$$

where $\mathbf{k} = (k_x, k_y, \omega)$ contains the zonal wavenumbers, meridional wavenumbers, and frequencies, respectively.

3.4 Performing the large- and small-scale parameter inference together

The objective of our multi-scale decomposition framework was to coherently separate each scale whilst acknowledging the characteristics of the other scales. We achieved this by inferring the seasonal model parameters, $\mathbb{E}[\mathbf{x}|\mathbf{y}]$, and rotational current covariance model parameters, θ, sequentially, a technique called block coordinate ascent. First θ was fixed and $\mathbb{E}[\mathbf{x}|\mathbf{y}]$ was inferred, then $\mathbb{E}[\mathbf{x}|\mathbf{y}]$ was fixed and θ was inferred. This sequence was iterated until convergence, usually three to five iterations. We used this technique because the structure of $\mathbf{H}\Sigma_{\mathbf{B}}\mathbf{H}^{\mathsf{T}} + \Sigma_{\mathbf{R}}$ was dense and therefore not appropriate to implement with Vecchia's approximation which presupposes intrinsic sparsity. An approximation of the posterior parameter distribution of θ was obtained after convergence using MCMC [described in Appendix D]. The complete workflow was:

1. Determine hyper-parameters for covariance matrix $\Sigma_{\mathbf{B}}$ and prior distributions for parameters in θ.
   (a) The hyper-parameters for $\Sigma_{\mathbf{B}}$ were never revised or optimised.
2. Estimate the seasonal model parameters $\mathbf{x}$ (Equation 4) and subtract the MAP estimate of $\overline{\mathbf{u}}$ from observations.
   (a) $\Sigma_{\mathbf{R}}$ was defined as a diagonal matrix with $\sigma = 0.1$ for the first iteration.

https://doi.org/10.5194/egusphere-2026-6450
Preprint. Discussion started: 3 November 2026
© Author(s) 2026. CC BY 4.0 License.

3. Optimise the parameters in θ by maximising the log-likelihood (Equation D2).
4. Take the MAP θ from step 3 and update $\Sigma_{\mathbf{R}}$. Repeat steps 2 and 3 until $\mathbb{E}[\mathbf{x}|\mathbf{y}]$ and θ converge. We determined convergence to be when the root-mean-square change of both θ and $\mathbf{x}$ was less then 0.005.
5. Run MCMC inference for θ after convergence. This provided posterior parameter uncertainty on the covariance model parameters. These parameters have physical significance and uncertainty quantification provides both physical and statistical insight.

There are three key components of uncertainty that are relevant to the framework and results. The first two components are the seasonal current prediction uncertainty [equation 5] and the rotational current prediction uncertainty [equation 10]. Velocity prediction 95% intervals were computed as ± 1.96 times the standard deviation of the prediction uncertainty. The third component is the uncertainty in our inferred rotational parameters, θ, herein parameter uncertainty, which was estimated from MCMC sampling. This inferred parameter uncertainty may have represented real variability, model misspecification, parameter identifiability issues, measurement error, or sparse sampling.

3.5 Making predictions

A key advantage of the GP framework is the ability to observe and predict from any space-time $\mathbb{R}^3 \to \mathbb{R}$ with quantified uncertainty. This allowed us to map sparse unstructured observations to unobserved points, such as a gridded field, making subsequent analyses easier. We can make predictions in space-time as

$$\mathbf{u}'^{*}_{p} = \Sigma_{po}\Sigma_{oo}^{-1}(\mathbf{y}'_{o}) \tag{9}$$

where the subscripts o and p indicate observation and prediction points respectively, and the * indicates an estimate conditioned on observations. Only the matrix Σ_{oo} includes the noise term, ϵ, on the diagonal. Vecchia's approximation was used to make the predictions with n_v=100. Extrapolating away from observations always comes with uncertainty, which should be considered to determine if the prediction is meaningful. The respective uncertainty estimate is

$$\Sigma^{*}_{pp} = \Sigma_{pp} - \Sigma_{po}\Sigma_{oo}^{-1}\Sigma_{op}. \tag{10}$$

4 Results

Seasonal currents were estimated at each observation coordinate and across a spatial grid over one year. Comparison of the results against the BRAN reanalysis outputs indicated low frequency flows had been suitably removed. Estimating the seasonal currents was not the objective of this work and therefore the relevant results can be found in Appendix E.

4.1 Inference and prediction validation

The GP regression results were inspected using standard stochastic modelling metrics. Quantile-quantile (QQ) and leave-one-drifter-out (LOO) predictions were performed to validate the covariance model using the MAP parameters [Figures 2

https://doi.org/10.5194/egusphere-2026-6450
Preprint. Discussion started: 3 November 2026
© Author(s) 2026. CC BY 4.0 License.

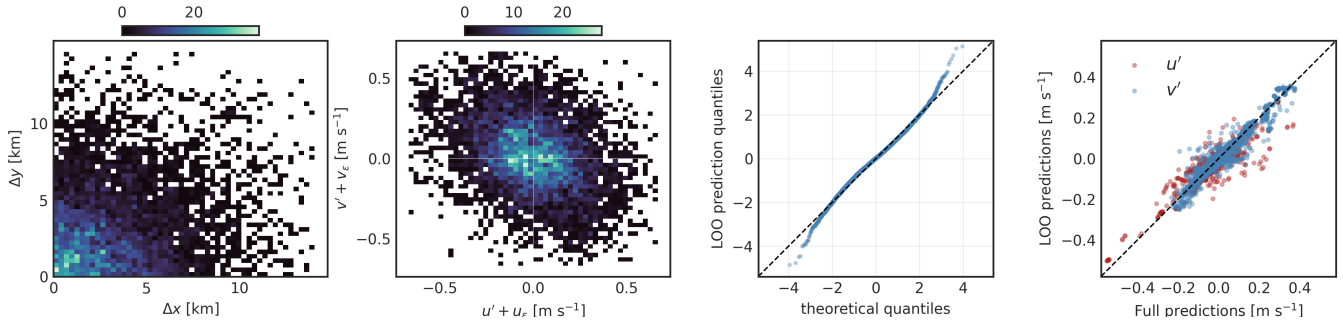


Figure 2. *Shelf* validation: (a) Distribution of drifter displacements in x and y in km (easting and northing). (b) Distribution of velocity observations with the seasonal currents removed. (c) QQ plot of uncertainty interval predictions normalised by theoretical quantiles (standardised normal distribution quantiles) against LOO observations. (d) GP velocity predictions against LOO observations that fall within ± 10 length scales of an included observation.

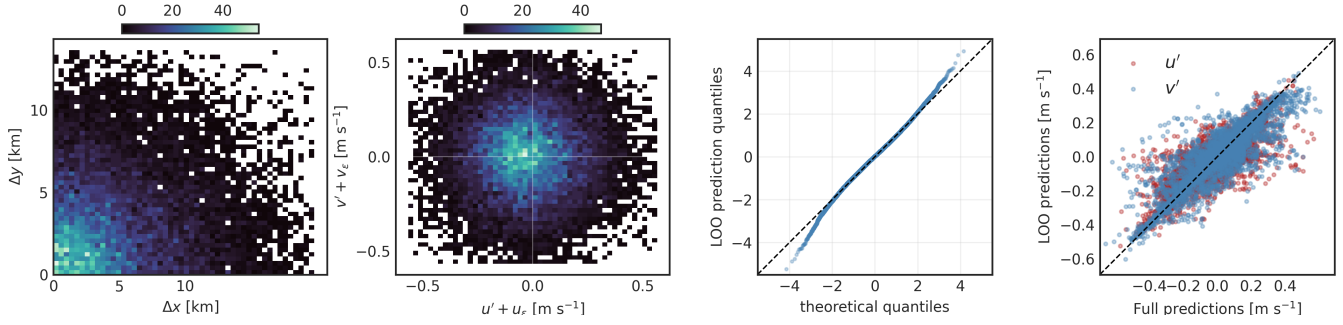


Figure 3. *Ocean* validation: (a) Distribution of drifter displacements in x and y in km (easting and northing). (b) Distribution of velocity observations with the seasonal currents removed. (c) QQ plot of uncertainty interval predictions normalised by theoretical quantiles (standardised normal distribution quantiles) against LOO observations. (d) GP velocity predictions against LOO observations that fall within ± 10 length scales of an included observation.

and 3]. QQ plots show that the majority of the uncertainty predictions were well-calibrated, but observation tails were larger than predicted by a normal distribution in both regions. This may be a legitimate feature of the observations which could be accounted for, but also could be driven by the sparse structure of the data and outlier comparisons. This does not bias the inferred MAP parameter values, but may indicate the MCMC parameter distributions are too narrow (overly confident).

Full vs. LOO predictions show good agreement with an expected level of variability when restricting the comparison to LOO coordinates within ± 10 length scales of an observation. We show the distribution of drifter displacements to confirm the small transverse length scales are still well-resolved. We also show the spatial distribution of observation displacements which confirm that the inferred length scales were well-resolved. In addition, we show the full distribution of observations used as inputs into the characterisation after the seasonal and Ekman currents were subtracted.

https://doi.org/10.5194/egusphere-2026-6450
Preprint. Discussion started: 3 November 2026
© Author(s) 2026. CC BY 4.0 License.

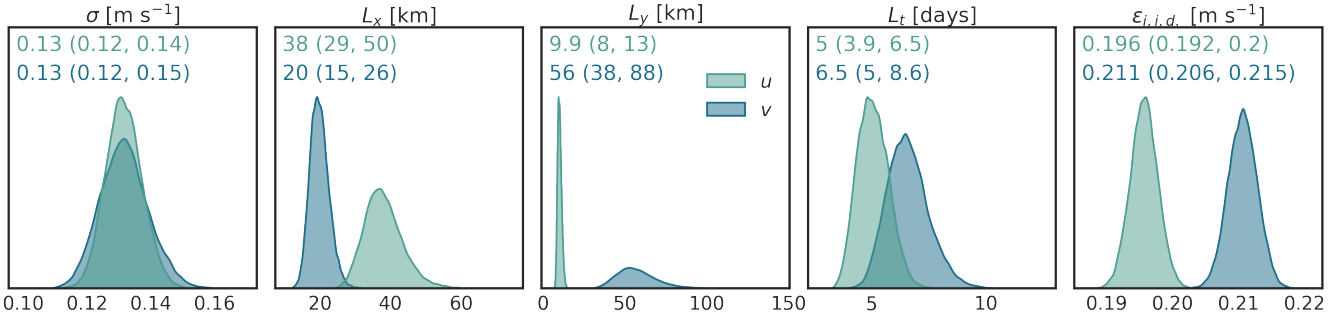


Figure 4. Inferred *shelf* posterior distributions of the covariance model parameters, θ, using MCMC for both the u' and v' components of the surface velocity. Text indicates the summary statistics: median (2.5%, 97.5% quantiles).

4.2 Characteristics of rotational motions

Rotational motions were statistically characterised for the *shelf* and *ocean* regions through the simultaneous estimation of their total energy and space-time length scales. The full posterior distributions for all parameters in θ from MCMC sampling had a clear peak for all parameters for both u' and v' inference [Figures 4 & 5]. Chain lengths were >50 times the auto-correlation length for all parameters and $\hat{R} \leq 1.05$ for all parameters [Appendix D].

The rotational motion σ was inferred with low uncertainty in both regions. *Ocean* σ was around 50% higher than on the *shelf*, or around twice as energetic. Agreement between the u and v components of σ for both regions provided further evidence that seasonal currents were sufficiently removed.

Inferred spatial scales were smaller on the *shelf* and larger in the *ocean* region. The longitudinal length scales for each velocity component, L_x for u' and L_y for v', were larger than the inferred transverse length scales, L_y for u' and L_x for v'. This anisotropy between spatial dimensions was an expected result of rotational motion behaviour [explored further in section 5.2]. Inferred u and v time scales were in agreement for the *ocean* region and smaller for u compared with v on the *shelf*. The cause of this difference in *shelf* time scales was not determined.

The inferred tidal frequency current standard deviation, $\epsilon_{i.i.d.}$, was stronger than σ on the *shelf*. This demonstrated the usefulness of the GP approach for low signal-to-noise applications, including multi-scale decompositions. Small differences in the u and v component estimates of $\epsilon_{i.i.d.}$ likely captured the dominance of meridional internal wave propagation in both regions (Gong et al., 2021).

Using the MAP parameters we computed the 2D frequency-wavenumber PSD from equation 8 [shown for the *shelf* region in Figure 6]. The more familiar marginal power spectra were computed for each dimension in both regions [Figure 7 & 8]. The MAP PSD were the most likely (best fit) results given our model choice and the observations. These conditioned models were a key outcome of the decomposition and inference framework described in this study. The impact of parameter uncertainty on the inferred PSD was quantified by drawing 1,000 samples from the MCMC posterior distributions, estimating each marginal spectra, and computing the 95% CI. This is fundamentally different to uncertainty in an empirical spectrum,

https://doi.org/10.5194/egusphere-2026-6450
Preprint. Discussion started: 3 November 2026
© Author(s) 2026. CC BY 4.0 License.

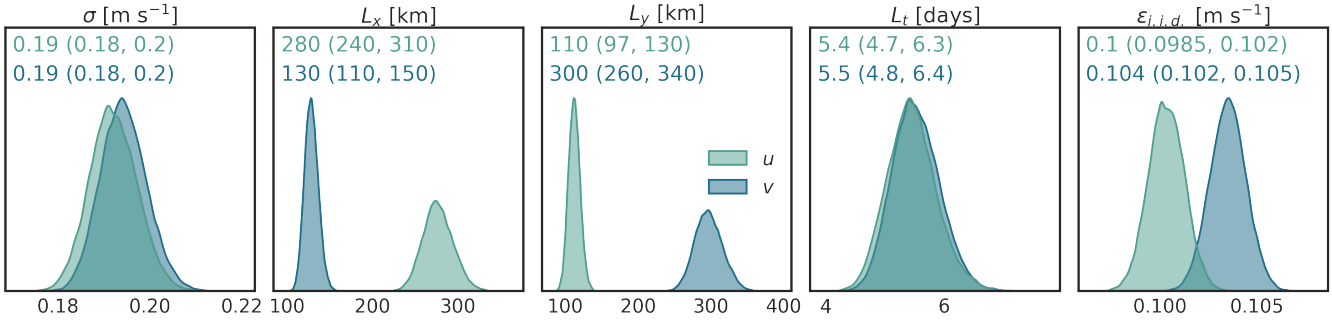


Figure 5. Inferred *ocean* posterior distributions of the covariance model parameters, θ, using MCMC for both the u' and v' components of the surface velocity. Text indicates the summary statistics: median (2.5%, 97.5% quantiles).

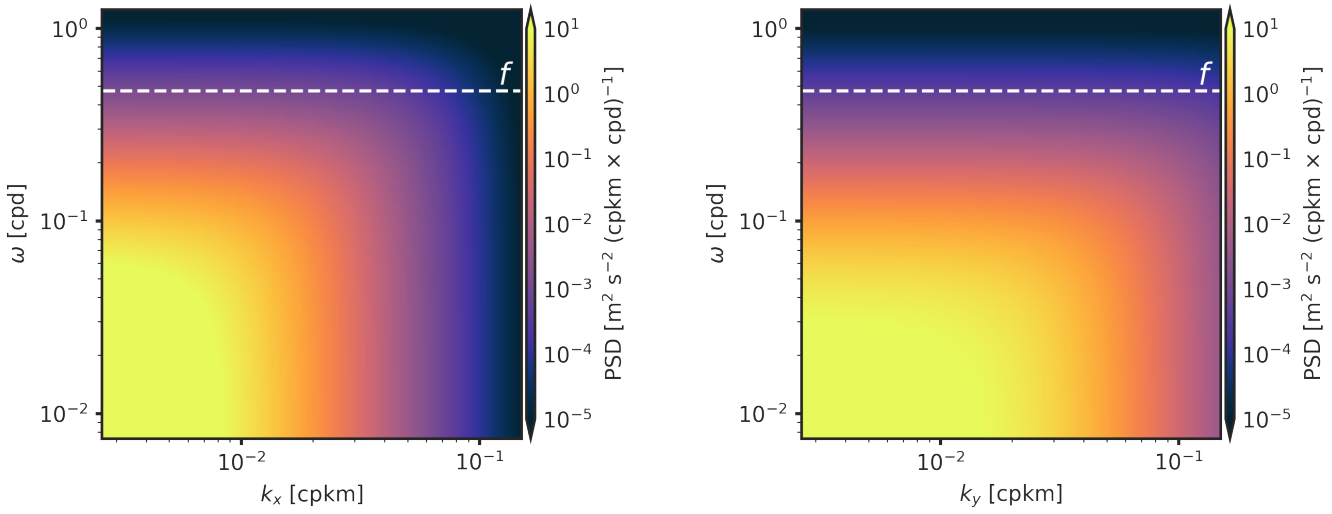


Figure 6. Inferred *shelf* u' PSD (using MAP parameters) shown for the $\omega - k_x$ and $\omega - k_y$ pairs marginalised (integrated) over the omitted dimension, k_y and k_x, respectively.

which usually captures sampling variability at each frequency or wavenumber. Here we are propagating uncertainty from the posterior distribution of θ. PSD uncertainty was (qualitatively) low in the *ocean* region despite the wide posterior distributions inferred for space and time scales.

4.3 Predictions capture a shelf eddy

265 The drifter dataset captured periods of interesting dynamics, particularly when several drifters were released in a short period. In one event, drifters on the *shelf* were advected around a strong coherent eddy, which left a clear fingerprint in the surface distribution of chlorophyll-a (Sentinel-3 imagery) [Figure 9g,h]. To examine this event we predicted the rotational motions,

https://doi.org/10.5194/egusphere-2026-6450
Preprint. Discussion started: 3 November 2026
© Author(s) 2026. CC BY 4.0 License.

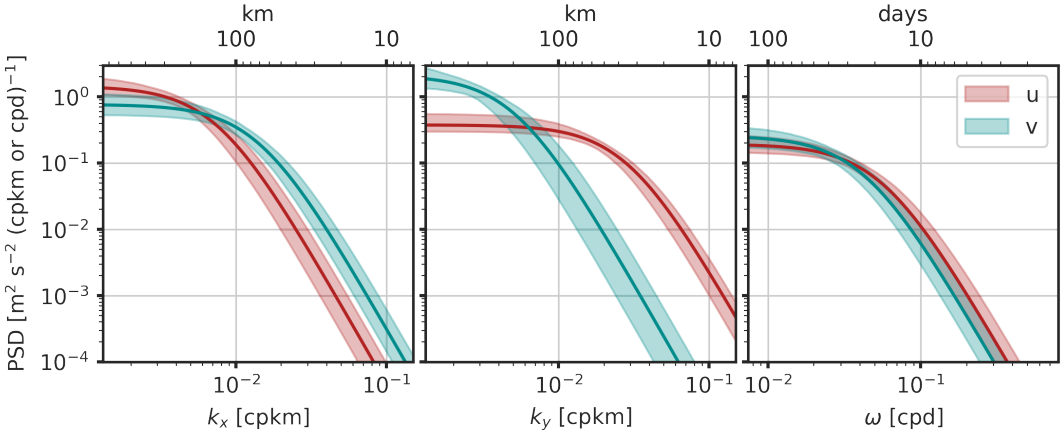


Figure 7. Inferred *shelf* PSD for each marginal dimension (integrated over the other two dimensions). The shaded region represents the 95% credible intervals due to parameter uncertainty from MCMC sampling. The slopes are fixed to -4 for each marginal spectrum using $C^{3/2}$ and the spectral roll-off is located at $\sim 1/2\pi L$ for cyclical frequencies.

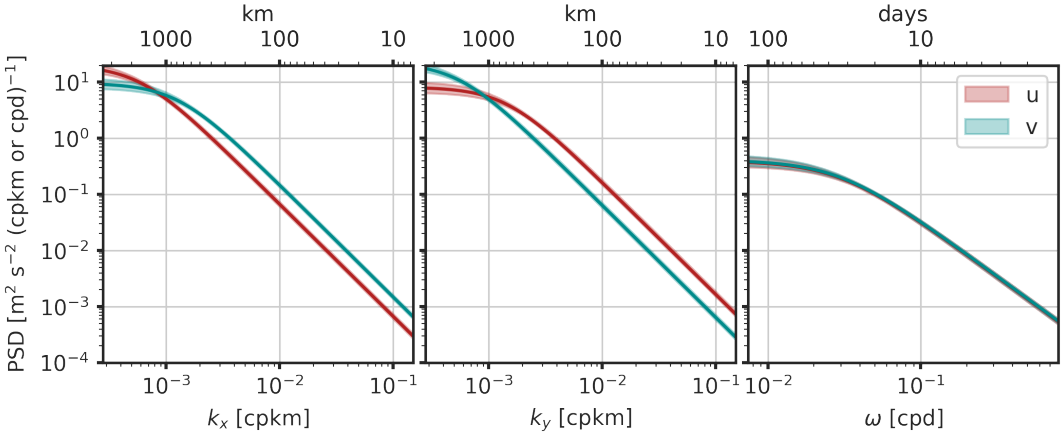


Figure 8. Inferred *ocean* PSD for each marginal dimension (integrated over the other two dimensions). The shaded region represents the 95% credible intervals due to parameter uncertainty from MCMC sampling. The slopes are fixed to -2 for each marginal spectrum using $C^{1/2}$ and the spectral roll-off is located at $\sim 1/2\pi L$ for cyclical frequencies.

https://doi.org/10.5194/egusphere-2026-6450
Preprint. Discussion started: 3 November 2026
© Author(s) 2026. CC BY 4.0 License.

i.e., the GP mean ($\mathbf{u'}^*_p$) and uncertainty (Σ^*_{pp}), from the drifter observations onto a regular spatiotemporal grid using Vecchia's approximation. The use of this approximation for predictions can introduce discontinuities between clusters of observations, where two extrapolated subsets meet. This is a known limitation that has been addressed in some extended methods, but here we simply increased the number of neighbours used for predictions to 100 to minimise the impact. The effect was still salient when taking the derivative of the velocity field [Figure 9c,d]. The prediction grid spacing was 6 hours and 2.5 km and spanned the duration of the dataset (∼3 years). Seasonal and unresolved (noise) currents were not included in this prediction. From the gridded fields we computed flow deformation properties, vorticity ζ, and divergence $\nabla \cdot \mathbf{u}'$. Note that GP mean predictions tend towards zero away from observations.

During this *shelf* event, three drifters observed a cyclonic eddy for at least 6 days in June 2023 [Figures 9]. From a zonal slice through the eddy at 14.2° S we inferred a sharp transition in v' velocity from 0.17 to -0.18 m s^{-1} over ∼22 km. Strong vorticity was inferred in the eddy centre, with the Rossby number, ζ/f, reaching 1.08. Uncertainty in the Rossby number was estimated by taking 100 random draws of u and v from the GP posterior, where each sample shows the behaviour of one possible realisation of the velocity field. The resulting uncertainty estimate had a standard deviation of ±0.13 at the eddy centre.

5 Discussion and further analysis

The inference and event predictions contain interesting features that we explore here to better understand the characterisation framework. First, we look closer at the predictions to verify if we have extracted the rotational currents. Next, we interpret the length and time scales to understand what they tell us physically about each region. Finally, we discuss some strengths and weaknesses of the method that enabled us to extract and characterise rotational motions and the implications for future work.

5.1 Extracting rotational motions

The GP mean predictions, $\mathbf{u}'$, and inferred flow deformation properties suggested our covariance model successfully extracted rotational currents from divergent ones, particularly tidal and internal wave motions. To confirm this we computed the rotational and divergent currents using the Helmholtz decomposition, giving $\mathbf{u'}_\psi$ and $\mathbf{u'}_\phi$ respectively. These were computed from the gridded velocity predictions from which we computed the stream and potential functions [Appendix F]. The mean HKE of $\mathbf{u'}_\psi$ was larger than $\mathbf{u'}_\phi$ in both regions, 73 vs 12 cm^2 s^{-2} on the *shelf* and 182 vs 34 cm^2 s^{-2} in the *ocean*. This contrast confirmed our covariance models and subsampling choices primarily captured rotational motions. The remaining divergent currents captured in $\mathbf{u}'$ were typically associated with strong rotational features [e.g., Figure 9] and were potentially prediction artefacts of our covariance model choice, which cannot strictly represent a nondivergent flow field (unlike Berlinghieri et al., 2023; Ponte et al., 2024). The spatial anisotropy also indicated successful capture of the rotational motions (discussed next).

https://doi.org/10.5194/egusphere-2026-6450
Preprint. Discussion started: 3 November 2026
© Author(s) 2026. CC BY 4.0 License.

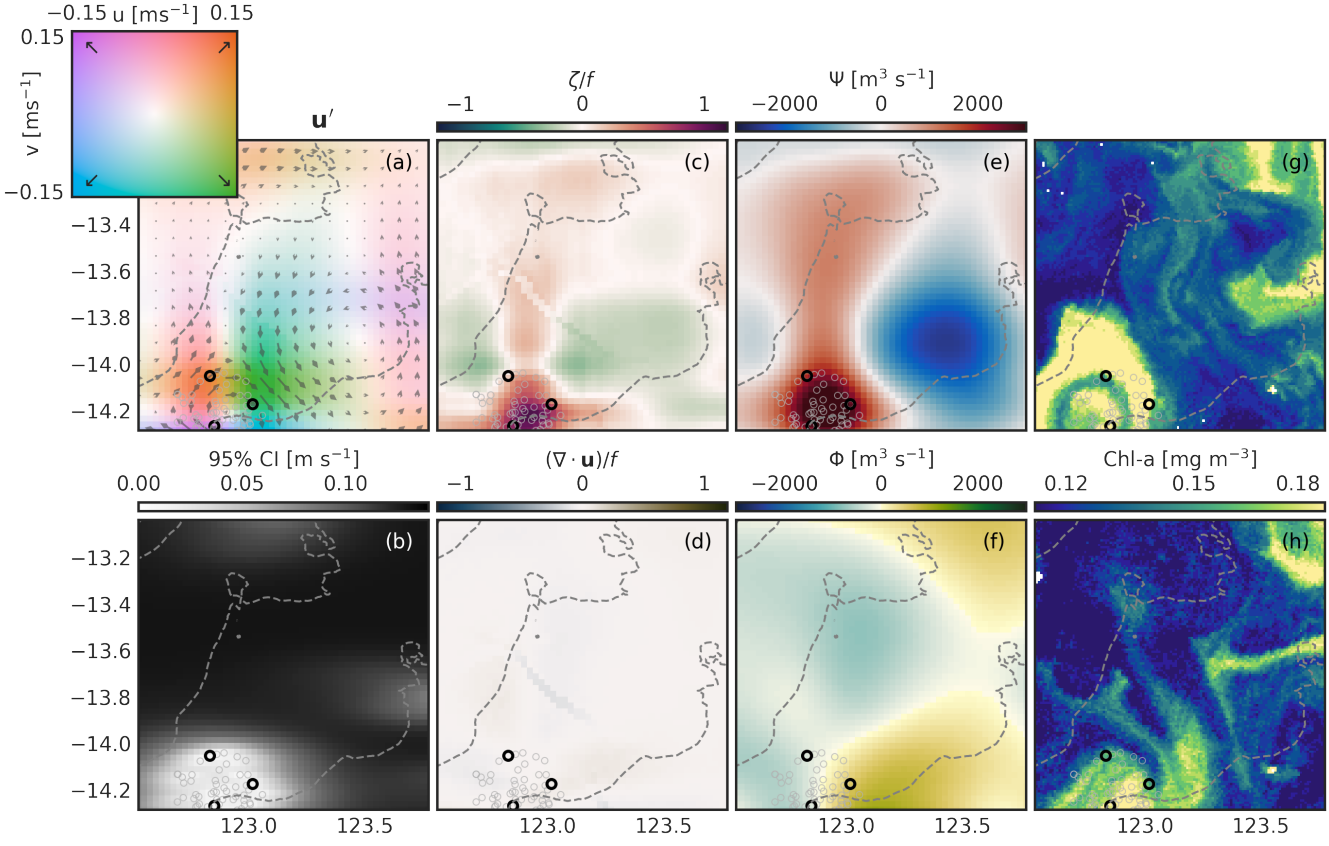


Figure 9. Drifters in the *shelf* region captured a cyclonic feature shown at 04:37 UTC on 25-06-2023. (a) The full field of predicted rotational motions. (b) The inferred uncertainty of the u' velocity component. (c) Estimated local Rossby number. (d) Estimated divergence scaled by the local inertial frequency. (e) Estimated stream function (ψ) and (f) potential function (ϕ). (g-h) chlorophyll-a (chl-a) concentration derived from Sentinel-3a images at 01:05 UTC on 20-06-2023 and 00:35 UTC on 25-06-2023, respectively, shown on the same colour scale. Light grey circles indicate the location of the three drifters within ± 3 days of the visualisation time. Artefacts of Vecchia's approximation can be seen, as a curved line to the southwest of the centre, in the Rossby number (e) and divergence (f) predictions where different subsets of observation clusters meet when extrapolated.

https://doi.org/10.5194/egusphere-2026-6450
Preprint. Discussion started: 3 November 2026
© Author(s) 2026. CC BY 4.0 License.

5.2 Interpreting the spatiotemporal scales

The inferred length scales were broadly in line with expectations from literature, but somewhat difficult to compare directly because (a) most studies do not attempt a dynamic decomposition prior to characterisation, and (b) some interpretation of the length scales is required before making any comparisons.

The observed spatial anisotropy in length scales is noted in oceanography literature. Scharffenberg and Stammer (2011) found anisotropy behaviour in the inferred zonal and meridional spatial scales of satellite-derived geostrophic velocities. Ubelmann et al. (2021, Figure 9) presented the geostrophic component of velocity fields which exhibits clear anisotropy. This behaviour can be attributed to 2D mass continuity (assuming incompressibility, Wunsch, 2015), which can be explained intuitively by the derivation of rotational currents from the stream function, $u = -\partial\psi/\partial y$ and $v = \partial\psi/\partial x$. For rotational currents we would not expect the same decorrelation behaviour for u when moving in the longitudinal (x) and transverse (y) dimensions.

This does not imply that the associated stream function was anisotropic. Middleton and Garrett (1986) derived the relation between the longitudinal and transverse velocity covariance functions, $\Sigma_{||}(r)$ and $\Sigma_{\perp}(r)$, at lag r, assuming isotropy. They showed that the transverse function relates to the longitudinal function as $\Sigma_{\perp}(r) = \Sigma_{||}(r) + r\partial\Sigma_{||}/\partial r$. Given we expect $\Sigma_{||}$ to decrease with r (moving away from zero) we would expect $\partial\Sigma_{||}/\partial r$ to be negative and $\Sigma_{||} > \Sigma_{\perp}$, in agreement with our inferred scales.

From the Middleton and Garrett (1986) relation we can derive the expected anisotropy ratios from matching e-folding distances for Matérn 1/2 and Matérn 3/2 functions representing purely nondivergent isotropic velocity fields to be $L_{||} = 2.31L_{\perp}$ and $L_{||} = 2.15L_{\perp}$, respectively. In the *ocean* region we inferred anisotropy ratios of 2.45 (2.22, 2.80) and 2.31 (2.05, 2.60) for u and v, respectively. This confirmed that the inference, which was free to choose any anisotropy, independently selected ratios consistent with a nondivergent field. The ratio is consistent with the hypothesis that the region's velocities were derived from an isotropic stream function. By contrast, anisotropy ratios on the *shelf* were 3.8 (2.8, 5.2), 2.8 (2.0, 4.8) for u and v, respectively. Departure from the expected ratio could indicate the capture of other processes by the kernel, or the influence of an anisotropic stream function, which is plausible given the potential for the shelf break to constrain and steer eddies in the region.

The MAP time scales were mostly between 5 and 6 days for u and v in both regions, with some posterior samples of up to 10 days inferred for the *shelf* v'. Time scales in this range are frequently associated with submesoscale processes. This conflicts with the inferred spatial scales, especially for the *ocean* region, which are associated with mesoscale eddies. In the *ocean* region we suspected the strong westerly ITF advection, which transported most of the drifters through the region, reduced the inferred time scales (Callies et al., 2020). This background advection of the rotational motions conflates true feature evolution with advective sweeping, in which advection drives apparent decorrelation as seen by an Eulerian observer (see Callies et al., 2020). Removal of the seasonal currents does not mitigate this effect.

Using the inferred time and length scales we can estimate the contribution of the evolution and advective components, assuming the time scales are composed as the sum of each component, $1/L_t = 1/T_{evo.} + 1/T_{adv.}$. Using the root-mean-square of the estimated ITF westward velocity, 0.23 m s^{-1}, computed for each drifter observation, together with the longitudinal

https://doi.org/10.5194/egusphere-2026-6450
Preprint. Discussion started: 3 November 2026
© Author(s) 2026. CC BY 4.0 License.

length scale for u' gives an estimate of the advective time scale, $T_{adv.} = L_s/U = 14.0$ days in the *ocean* region. Substituting this to compute the evolution time scale gives an estimated $T_{evo.} = 8.8$ days and indicates advection is responsible for 39% of the observed decorrelation for *ocean* u' velocity. A similar result of 39% was obtained for *ocean* v' velocity if we assume the longitudinal scale is the appropriate scale to represent the characteristic feature structure which is advected by low frequency flow, but the analysis fails if we use the shorter transverse scales. Using a characteristic advection speed of 0.05 m s^{-1} and the longitudinal scales for the *shelf*, we estimated that advection accounted for an estimated 57% and 40% of the observed decorrelation for u and v, respectively. This heuristic analysis could be confirmed by covariance modelling that includes an advective term, but we leave this to future work.

5.3 Methodological opportunities and constraints

The framework presented here can be used with any valid covariance model, if the model's parameters are identifiable given the observations. We chose Matérn models to represent the rotational motion spectral frequency-wavenumber cusp because they are relatively simple (when ν is fixed), have linear tails in log-log space and have analytical covariance and spectral forms. The Matérn 1/2 and 3/2 are both simplifications of the spectral cusp observed in numerical model analyses (Torres et al., 2018). We tested a covariance model with 3D rotation parameters to simulate space-time propagation but the additional parameters were poorly identified in the inference and did not substantially increase the likelihood.

The GP inference framework contained two key assumptions, (1) that the field is joint multivariate normal, and (2) that its covariance takes a Matérn form. Calibration indicated that the observations deviated from a normal distribution with heavier tails. The GP likelihood only depends on the first and second moments of the observations so the inferred parameters in θ will remain consistent in this case assuming the specified Matérn is adequate (Guyon, 1982). The non-Gaussian observations instead affects the uncertainty quantification, both for parameter uncertainty and prediction intervals, which will both be underestimated.

The results have demonstrated that this method can approximately decompose and characterise rotational motions from in-situ observations. We applied this framework to drifter-derived velocities, but the framework is observation platform independent and could be used to infer statistical properties from aggregated datasets. Improvements could be made by modelling the bivariate velocity field (u, v) together as their correlation provides additional information (Berlinghieri et al., 2023; Ponte et al., 2024). Using these rotational and divergent covariance models with this framework could open the possibility of combining in-situ velocity and satellite altimetry data for inference and prediction.

We attempted to fit the Matérn 1/2 covariance model to the shelf observations with the assumption that a spectral slope of -2 would most accurately represent the physical process of interest. This approach inferred short time scales (<1 day) driven by high frequency variability that were not fully captured with an i.i.d. noise term. Instead we fit a (more forgiving) Matérn 3/2 covariance model and inferred time scales representative of shelf rotational motions. The energetic $\epsilon_{i.i.d.}$ component may have contributed to why we could not fit a Matérn 1/2 to the *shelf* observations. Explicit treatment of the tidal frequency component with its own covariance model may further improve the inference and permit the inclusion of higher temporal resolution observations.

https://doi.org/10.5194/egusphere-2026-6450
Preprint. Discussion started: 3 November 2026
© Author(s) 2026. CC BY 4.0 License.

6 Conclusions

We were successfully able to infer the joint 3D space and time scales of rotational surface velocities from unstructured drifter observations. Results indicate that the application of this approach, following Ponte et al. (2024), to in-situ ocean observations is suitable when competing processes were considered (in this case low frequency and tidal frequency motions). We inferred the characteristic parameter set, including spatial anisotropy, from relatively small datasets in a way that standard binned approaches cannot. The framework provides simultaneous characterisation and decomposition of the observations which are useful for both scientific interpretation and operational applications. The framework also identified coherent uncertainty on the joint parameter set, which highlighted the inherent uncertainty in the inferred spatial scales and allowed for trivial uncertainty propagation into further analysis.

The GP framework was useful for performing both the multi-scale decomposition and inference of rotational flows in low signal-to-noise environments. Inferred *shelf* rotational motion energy was much smaller than the tidal and supertidal energy. Inferred spatial scales were anisotropic but consistent with rotational velocity field characteristics. The *shelf* and *ocean* regions exhibited distinct spatial scales as expected, but had similar temporal scales, both driven by a mix of advective decorrelation and temporal evolution. The divergent component of the extracted rotational motions was small, confirming the inferred scales were representative of the intended process.

The GP approach is computationally intensive, particularly for the inference, but was improved through the implementation of Vecchia's approximation. Many previous studies have approached characterisation work with a collection of different methods and independent (or lacking) uncertainty estimates. Here, the framework jointly inferred the characteristics and uncertainty with a coherent covariance model approach. The framework is not location, process, or observation platform specific, but instead modular in nature due to the additive property of covariance. We intend to use this framework for future work combining multiple processes and observation types.

Multi-platform multi-scale assimilation approaches are becoming more important as we try to synthesise global remote-sensing and in-situ data at higher resolutions to understand the spatiotemporal variability of the ocean. The results of this study demonstrate the potential for applying more advanced methods such as bivariate (u, v) and stream function covariance modelling. Combining SWOT wide-swath altimetry with in-situ observations presents an opportunity to better understand small-scale processes. This also necessitates investigations on the appropriate representations of the 3D internal gravity wave spectrum that often dominates observations on smaller scales. The developments presented here may help provide a pathway towards decomposition and characterisation of observations from multi-platform datasets.

Code and data availability. The full drifter dataset can be found online (Pattiaratchi, 2025). The subsampled data and all relevant code can be found at https://github.com/williamedge/drifterOI-public (this will be archived to Zenodo after peer review).

https://doi.org/10.5194/egusphere-2026-6450
Preprint. Discussion started: 3 November 2026
© Author(s) 2026. CC BY 4.0 License.

Appendix A: Vecchia's approximation overview

Computation of the likelihood and making predictions both require inverting Σ, which has size $n \times n$, where n is the number of observations. For dense covariance matrices computation cost scales by $\mathcal{O}(n^3)$. This means repeated inference and even single predictions become intractable when n is larger than $10^3 - 10^4$.

Recent developments in the statistical literature based on Vecchia's approximation to a Gaussian process (Vecchia, 1988; Katzfuss and Guinness, 2021) enable GP applications to larger datasets. Instead of evaluating the full likelihood, Vecchia approximates it as the product of many small conditional distributions [equations A1 and A2]. The size of each conditional distribution, n_v, represents the number of nearest neighbours selected in the computation, effectively truncating the dense Σ. This sparsity breaks a single large $\mathcal{O}(n^3)$ computation into many small $\mathcal{O}(n_v^3)$ computations, with costs now scaling by $\mathcal{O}(n \cdot n_v^3)$. Each conditional distribution only depends on its local neighbour subset and these computations can be performed in parallel. The key choice to make when using Vecchia's approximation is the size of the local subsets, n_v, which dictates a trade off between accuracy, increasing with larger n_v, and computation time, increasing with larger n_v. In practice, Vecchia's approximation can closely reproduce the exact likelihood with as few as 30 neighbours (Guinness, 2018).

For any ordering of our n observations, $\mathbf{y}'$, the exact log-likelihood (Equation D2) can be written without approximation as a sum of n univariate conditional log-densities,

$$\log\, p(\mathbf{y}'|\theta) = \sum_{i=1}^{n} \log\, p\big(y'_i \mid y'_1, ..., y'_{i-1}; \theta\big), \tag{A1}$$

where each conditional density is itself Gaussian, with a mean and variance given by standard GP conditioning. Evaluating Equation A1 exactly is worse than the original $\mathcal{O}(n^3)$ problem because the ith conditioning set grows to size $i-1$. Vecchia (1988) instead approximates each term by conditioning y'_i on only its n_v nearest neighbours, $c(i) \subset \{1, ..., i-1\}$, ranked by the scaled distance d (Equation 7),

$$\log\, p(\mathbf{y}'|\theta) \approx \sum_{i=1}^{n} \log\, p\big(y'_i \mid \mathbf{y}'_{c(i)}; \theta\big). \tag{A2}$$

Each term in Equation A2 now requires inverting only an $n_v \times n_v$ matrix rather than one $n \times n$ matrix, reducing the total cost from $\mathcal{O}(n^3)$ to $\mathcal{O}(n \cdot n_v^3)$, and the n terms are conditionally independent given θ so can be evaluated in parallel. Unlike a time series, spatiotemporal observations have no natural ordering, so both the ordering of the y'_i and the neighbours selected for $c(i)$ influence the accuracy of Equation A2 for a given n_v; we used nearest-neighbour conditioning sets under a random ordering, following the general framework and accuracy comparisons of orderings and neighbour-selection schemes in Katzfuss and Guinness (2021). The same nearest-neighbour approximation applies to the conditional (predictive) distributions used for mapping (Section 3.5).

Appendix B: Drifter data quality control

The drifters uploaded GPS position coordinates at approximately 5 minute intervals. If an upload was interrupted the position data could be uploaded later with an incorrect time stamp, resulting in bad velocity estimates. Bad position data was removed

https://doi.org/10.5194/egusphere-2026-6450
Preprint. Discussion started: 3 November 2026
© Author(s) 2026. CC BY 4.0 License.

using an unstructured version of the method described in Goring and Nikora (2002). This involved the subtraction of low frequency position changes using a boxcar filter with a short (3-point) window then computation of the first and second time derivatives (velocity and acceleration). The short filter window was used to remove the non-stationarity present in the drifter-derived velocity and acceleration estimates. This de-spiking method is based on the 3D ellipsoid (position, velocity, acceleration) computed using the expected absolute maximum value for each axis assuming all three quantities are normally distributed random variables. Points outside the ellipsoid were removed without replacement and the derivatives computed again until no outliers were detected. The de-spiking was run independently for zonal and meridional position and coordinates were removed from the analysis if an outlier was detected in either component. Zonal and meridional velocity were re-computed after de-spiking was complete. This method can fail when coordinates are isolated and unphysical changes in position, velocity and acceleration cannot be detected. Manual flagging was also performed after the de-spiking method and suspicious isolated observations were removed.

Appendix C: Seasonal harmonic model

The seasonal currents, $\overline{\mathbf{u}} = \mathbf{H}\mathbf{x}$ (Eq. 4), were modelled independently for u and v as a time series, with annual and semi-annual harmonics at frequency $\omega = 2\pi/T$ and 2ω, respectively, where $T = 365.25$ days. For an observation at time t_i, the corresponding row of the harmonic model operator was

$$\mathbf{h}(t_i) = \left[1,\ \cos(\omega t_i),\ \sin(\omega t_i),\ \cos(2\omega t_i),\ \sin(2\omega t_i)\right], \tag{C1}$$

where the full $\mathbf{H}$ has the compact form

$$\mathbf{H} = \left[D_1, D_2, D_3, D_4, D_5\right], \qquad D_j = \mathrm{diag}(h_j(t_1), ..., h_j(t_n)). \tag{C2}$$

The corresponding parameter vector is $\mathbf{x} = [\mathbf{x}_0^\mathsf{T}, \mathbf{x}_1^\mathsf{T}, \mathbf{x}_2^\mathsf{T}, \mathbf{x}_3^\mathsf{T}, \mathbf{x}_4^\mathsf{T}]^\mathsf{T}$, with each $\mathbf{x}_j \in \mathbb{R}^n$, containing the mean ($\mathbf{x}_0^\mathsf{T}$) and the annual and semi-annual amplitude coefficients. This five-coefficient form including the mean (Equation C1) was used for the *ocean* region. For the *shelf* region the mean column was dropped giving the four-coefficient form

$$\mathbf{h}(t_i) = \left[\cos(\omega t_i),\ \sin(\omega t_i),\ \cos(2\omega t_i),\ \sin(2\omega t_i)\right], \qquad \mathbf{x} = [\mathbf{x}_1^\mathsf{T}, \mathbf{x}_2^\mathsf{T}, \mathbf{x}_3^\mathsf{T}, \mathbf{x}_4^\mathsf{T}]^\mathsf{T}. \tag{C3}$$

Mooring records from the region suggest any net mean flow is weak. Thus the *shelf* mean flow was not well constrained by the observations and its inclusion degraded the fit. $\mathbf{H}$ was applied separately to u and v, giving independent parameter vectors $\mathbf{x}_u$ and $\mathbf{x}_v$. Note the spatial variation of each harmonic coefficient was constrained through the *a priori* covariance $\Sigma_\mathbf{B}$ (Section 3.2).

Seasonal currents were mapped onto a regular grid by first predicting the coefficient fields at the grid locations, $\Sigma_{\mathbf{B},po} = \mathrm{diag}(\sigma^2_{\mathbf{B},1}, ..., \sigma^2_{\mathbf{B},5}) \otimes \mathbf{K}_s(s_p, s_o)$. The posterior coefficient fields and error covariance were then computed as

$$\mathbb{E}[\mathbf{x}_p|\mathbf{y}] = \Sigma_{\mathbf{B},po}\mathbf{H}^\mathsf{T}\left(\mathbf{H}\Sigma_\mathbf{B}\mathbf{H}^\mathsf{T} + \Sigma_\mathbf{R}\right)^{-1}\mathbf{y}, \tag{C4}$$

https://doi.org/10.5194/egusphere-2026-6450
Preprint. Discussion started: 3 November 2026
© Author(s) 2026. CC BY 4.0 License.

$$\mathbb{V}[\mathbf{x}_p] = \Sigma_{\mathbf{B},pp} - \Sigma_{\mathbf{B},po}\mathbf{H}^\mathsf{T}\left(\mathbf{H}\Sigma_\mathbf{B}\mathbf{H}^\mathsf{T} + \Sigma_\mathbf{R}\right)^{-1}\mathbf{H}\Sigma_{\mathbf{B},op}. \tag{C5}$$

These reduce to equations 4 and 5 when $s_o = s_p$.

Appendix D: MCMC implementation and convergence details

Bayesian MCMC Motivations

By modelling our ocean observations, $\mathbf{y}$, as a statistical process with covariance kernel, $c(\mathbf{z}, \mathbf{z}'; \theta)$ (herein $c(\theta)$) with model parameters in θ, we can compute a likelihood function, $p(\mathbf{y}|\theta)$. The likelihood quantifies the probability of observing $\mathbf{y}$, given our statistical model, $c(\theta)$. Frequentist optimisation of $p(\mathbf{y}|\theta)$ treats θ as unknown but fixed. Bayesian inference treats θ as inherently uncertain. Bayesian inference also coherently incorporates prior beliefs on θ, $p(\theta)$, into an updated posterior belief, $p(\theta|\mathbf{y})$. These two features are ideal for oceanographic inference problems, where often a large body of literature informs our choices and the underlying process may vary slightly in space or time. Bayes theorem lets us compute the posterior as

$$p(\theta|\mathbf{y}) = \frac{p(\theta)p(\mathbf{y}|\theta)}{p(y)} \propto p(\theta)p(\mathbf{y}|\theta). \tag{D1}$$

The posterior summarises the updated degree of belief in θ, which is treated as a distribution rather than a single point estimate.

Oceanographic observations and inverse problems are inherently uncertain. The combination of instrument error, sampling design, statistical model choice, incomplete data decomposition, and real physical variability of a process contribute to uncertainty in the estimate of θ. Often only single point estimation is performed, either in a frequentist framework (maximum likelihood estimation or MLE) or a Bayesian framework (maximum a posteriori or MAP). Single point estimates of max $p(\theta|\mathbf{y})$ can hide significant uncertainty and even identifiability issues. Critically, single point estimates cannot be used to propagate parameter uncertainty into further analysis.

Markov-Chain Monte Carlo (MCMC) methods are used to computationally explore the posterior distribution of $p(\theta|\mathbf{y})$ when it is analytically intractable. Critically, MCMC methods bypass the need to compute $p(y)$, which is generally the intractable component, by generating proportional posterior estimates, $p(\theta)p(\mathbf{y}|\theta)$. A chain of parameters is proposed and $p(\theta)p(\mathbf{y}|\theta)$ is evaluated. From the current θ_0 a new θ_1 is proposed and $p(\theta)p(\mathbf{y}|\theta)$ is computed for both. The proposed θ_1 is accepted or rejected with a probability that favours a higher posterior probability, while still permitting occasional moves towards a lower probability. Repetition of this proposal of parameters generates the Markov chain of θ

Once iterative estimates of $\mathbb{E}[\mathbf{x}|\mathbf{y}]$ converged and $y' = y - \mathbb{E}[\mathbf{x}|\mathbf{y}]$ was computed we inferred the posterior distribution of each parameter in θ and their covariance using MCMC (full workflow in Section 3.4). MCMC and MAP inference require computation of the log-likelihood of our observations given our parameters (and model choice),

$$\log\, p(\mathbf{y}'|\theta) = -\frac{1}{2}\log|C(\theta)| - \frac{1}{2}(\mathbf{y}')^\top C(\theta)^{-1}(\mathbf{y}') + const. \tag{D2}$$

where the constant does not depend on θ. The product of the likelihood and our chosen priors for θ gives the final posterior density. The priors for θ were chosen based on literature and informed by our knowledge from research in both regions [Table

https://doi.org/10.5194/egusphere-2026-6450
Preprint. Discussion started: 3 November 2026
© Author(s) 2026. CC BY 4.0 License.

1]. We used Vecchia's approximation to compute the log-likelihood with the subset size, n_v, set to 30. The priors were designed to be informative, limiting the tendency to attribute all observed variance to the noise term or to a spatial only process. With the exception of $\epsilon_{i.i.d.}$ and L_t priors were all half-normal with a mean and standard deviation, e.g., $|\mathcal{N}(\mu,\sigma)|$. The priors for $\epsilon_{i.i.d.}$ and L_t were a log-normal, $\ln\mathcal{N}(\mu,\sigma)$, to prevent the inference from fitting all variance to the spatial component only with no time dependency. The priors for L_x and L_y were designed to limit the GP from absorbing seasonal signal.

MCMC was run using the affine invariance ensemble sampler using Python's *emcee* package (Goodman and Weare, 2010; Foreman-Mackey et al., 2013). We ran the ensemble sampler with 25 walkers for 1000 burn-in samples and 5,000 further iterations each, producing 125,000 samples of the posterior. This method converges on the posterior because walkers transfer information on the posterior features to each other. We computed standard checks of the integrated autocorrelation time and the number of effective samples (Section 4.2). Uncertainty quantification of the posterior parameter distributions using credible intervals (CI) are computed directly from the MCMC samples. For example, the 95% intervals (a,b) of θ are the probability $p(a<\theta<b|\mathbf{y})=0.95$.

Proposal and acceptance

The posterior of θ was sampled separately for each of the four analyses (*shelf* u', *shelf* v', *ocean* u', *ocean* v') using the affine-invariant ensemble sampler of Goodman and Weare (2010), implemented in `emcee` (Foreman-Mackey et al., 2013). At each iteration, a walker $\mathbf{X}_k$ is updated using the "stretch move": a second walker $\mathbf{X}_j$ is drawn at random from the remaining ensemble and a candidate is proposed as

$$\mathbf{X}_k(t+1)=\mathbf{X}_j+z\big[\mathbf{X}_k(t)-\mathbf{X}_j\big], \tag{D3}$$

where the stretch factor z is drawn from $g(z)\propto 1/\sqrt{z}$ for $z\in[1/a,a]$, with the scale parameter $a=2$ (the `emcee` default). The candidate is accepted with probability

$$\min\Big(1,\ z^{K-1}\,\frac{p(\mathbf{X}_k(t+1)|\mathbf{y}')}{p(\mathbf{X}_k(t)|\mathbf{y}')}\Big), \tag{D4}$$

where $K=5$ is the number of parameters in θ and $p(\cdot|\mathbf{y}')$ is the Vecchia-approximated posterior density (Equation D2). Unlike single-chain Metropolis–Hastings, the stretch move (Equation D3) uses the instantaneous spread of the ensemble to inform each proposal, which improves mixing when parameters (e.g. L_x, L_y, L_t) are correlated. We ran 25 walkers for 1000 burn-in iterations (discarded), followed by 5000 sampling iterations, giving 25×5000 =125,000 posterior samples per analysis.

Convergence diagnostics

Convergence was assessed for every parameter in θ, in all four analyses, using the potential scale reduction factor, $\hat{R}$ (Gelman and Rubin, 1992), and the integrated autocorrelation time, τ. Treating the $m=25$ walker chains (post burn-in, length n) as independent chains, $\hat{R}$ is

$$\hat{R}=\sqrt{\frac{\hat{V}}{W}},\qquad \hat{V}=\frac{n-1}{n}W+\frac{1}{n}B, \tag{D5}$$

https://doi.org/10.5194/egusphere-2026-6450
Preprint. Discussion started: 3 November 2026
© Author(s) 2026. CC BY 4.0 License.

Table D1. MCMC convergence diagnostics for each analysis, reported as the maximum $\hat{R}$, maximum τ, and minimum ESS all walkers, reported for each of the five parameters in θ.

Analysis	$\hat{R}$ (max)	τ (max)	ESS (min)
Shelf u'	[1.012, 1.013, 1.015, 1.015, 1.016]	[64, 61, 61, 65, 77]	[1951, 2040, 2050, 1936, 1624]
Shelf v'	[1.011, 1.012, 1.021, 1.017, 1.019]	[62, 59, 58, 72, 68]	[2027, 2125, 2153, 1734, 1843]
Ocean u'	[1.014, 1.012, 1.013, 1.014, 1.016]	[59, 59, 61, 65, 59]	[2118, 2132, 2038, 1932, 2128]
Ocean v'	[1.016, 1.020, 1.018, 1.020, 1.014]	[53, 62, 58, 63, 62]	[2351, 2019, 2171, 1973, 2012]

where W and B are the average within-chain and between-chain variances of the parameter, respectively. $\hat{R} \to 1$ as the chains converge to the same stationary distribution. The integrated autocorrelation time,

$$\tau = 1 + 2\sum_{k=1}^{\infty} \rho(k), \tag{D6}$$

with $\rho(k)$ the chain autocorrelation at lag k, quantifies the number of iterations between effectively independent samples and gives the effective sample size, ESS $= nm/\tau$. We required $\hat{R} \leq 1.05$ and a chain length of at least 50τ for every parameter to accept convergence [Table D1].

Appendix E: Seasonal current predictions

Seasonal currents, $\overline{\mathbf{u}}$, were predicted on a regular spatial grid over one year for both the *shelf* and *ocean* regions [Figure E1 and Figure E2]. 30 years of gridded re-analysis currents from Bluelink (Chamberlain et al., 2021) were fit to the same seasonal harmonic model for comparison. We averaged predictions over the indigenous Yawuru seasons which better reflect the region's seasonal patterns.

Predictions in the *shelf* region captured the South-westerly Leeuwin current Kelvin wave (Ridgway and Godfrey, 2015) in April-June and its reversal in July-September [Figure E1]. The clear semi-annual signal in the BRAN seasonal currents was only weakly captured by the drifters [Figure E3].

Predictions in the *ocean* region captured the strong Indonesian through-flow (ITF) that occurs outside of the Austral summer [Figures E2 and E3]. When the ITF stops from December-March seasonal currents were weaker and agreement with BRAN was less clear. Uncertainty in the region was lower compared to the maximum amplitudes, but still significant. The spatial distribution of uncertainty reflected the sampling pattern of the drifters, showing higher uncertainty in the poorly observed south-east corner of the *ocean* region.

https://doi.org/10.5194/egusphere-2026-6450
Preprint. Discussion started: 3 November 2026
© Author(s) 2026. CC BY 4.0 License.

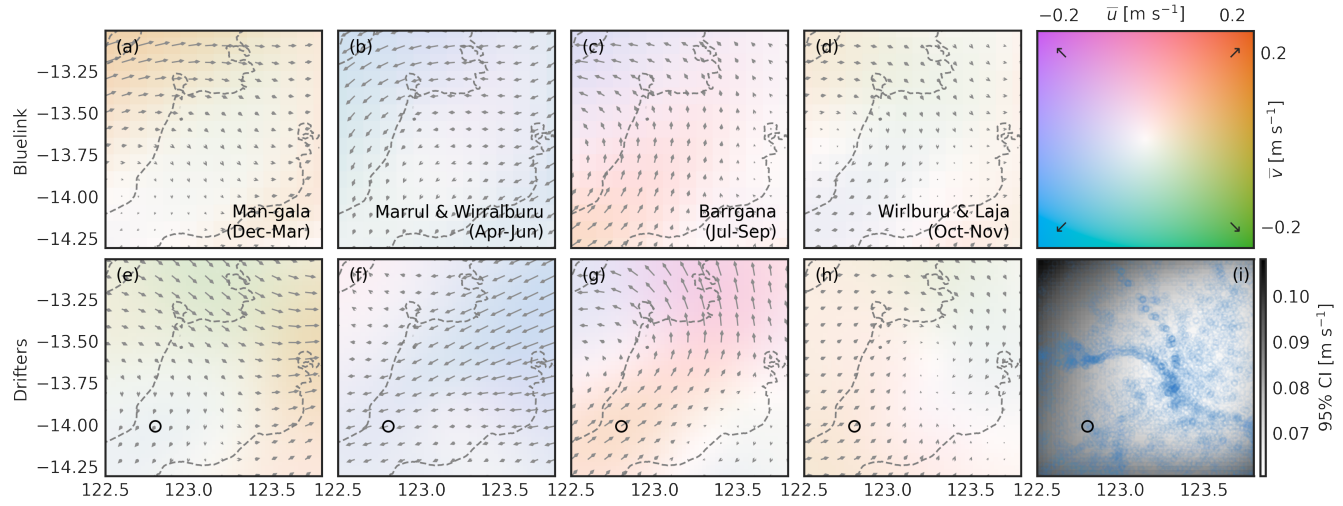


Figure E1. (a-d) Seasonal currents in the *shelf* region from the Bluelink 30-year data-assimilating re-analysis product (BRAN) averaged over the local Yawuru seasons. (e-h) Inferred seasonal currents from the drifters for the same region and seasons as above. (i) the spatial distribution of uncertainty for the seasonal current velocity at 2020-01-01 ($\overline{u}$ and $\overline{v}$ spatial uncertainty of seasonal currents were equal). The black circle indicates the location of the time series in Figure E3. Current velocity colours shown in the top right panel.

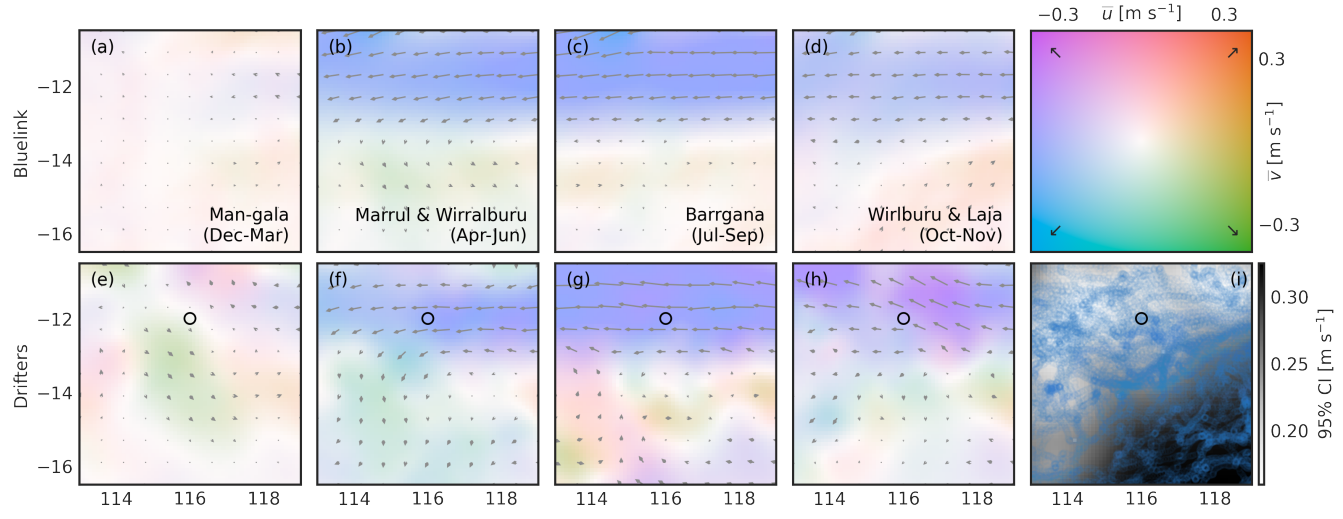


Figure E2. (a-d) Seasonal currents in the *ocean* region from the Bluelink 30-year data-assimilating re-analysis product (BRAN) averaged over the local Yawuru seasons. (e-h) Inferred seasonal currents from the drifters for the same region and seasons as above. (i) the spatial distribution of uncertainty for the seasonal current velocity at 2020-01-01 ($\overline{u}$ and $\overline{v}$ spatial uncertainty of seasonal currents were equal). The black circle indicates the location of the time series in Figure E3. Current velocity colours shown in the top right panel.

https://doi.org/10.5194/egusphere-2026-6450
Preprint. Discussion started: 3 November 2026
© Author(s) 2026. CC BY 4.0 License.

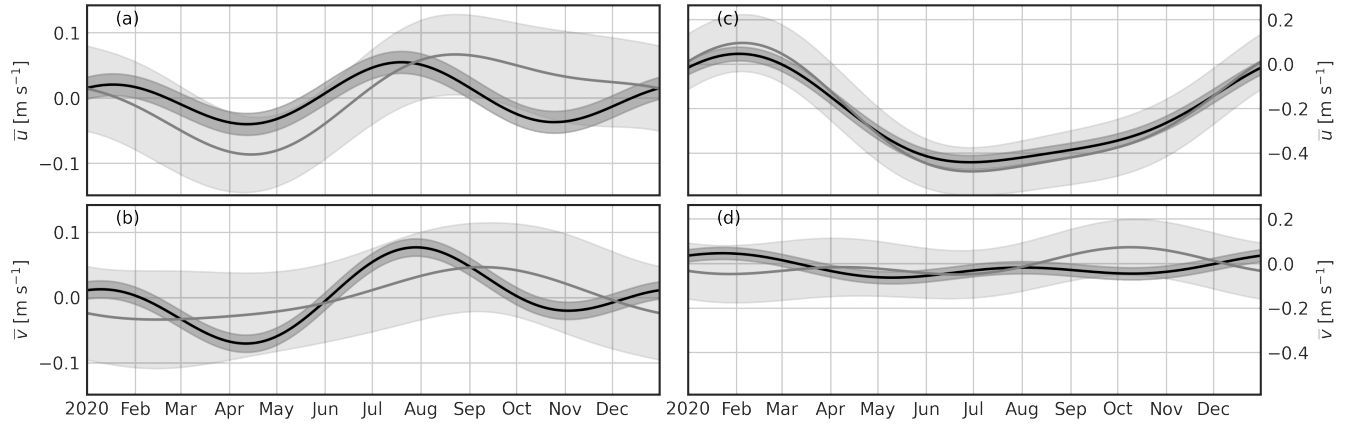


Figure E3. (a-b) Seasonal currents in the *shelf* region at 122.8° E, 14° S, estimated from the drifters (grey) and from BRAN (black). (c-d) Seasonal currents in the *ocean* region at 116° E, 12° S, estimated from the drifters (grey) and from BRAN (black). Shading around each line indicates the 95% credible intervals.

Appendix F: Stream and potential functions and Helmholtz decomposition

The gridded rotational current predictions, $\mathbf{u'}^{*}_{p} = (u', v')$ (Section 3.5), were decomposed at each output time step into a rotational (non-divergent) component, $\mathbf{u'}_{\psi}$, and a divergent (irrotational) component, $\mathbf{u'}_{\phi}$, via the Helmholtz decomposition, $\mathbf{u'} = \mathbf{u'}_{\psi} + \mathbf{u'}_{\phi}$. The relative vorticity, $\zeta = \partial v'/\partial x - \partial u'/\partial y$, and the divergence, $\delta = \partial u'/\partial x + \partial v'/\partial y$, were computed from $\mathbf{u'}^{*}_{p}$ using centred finite differences. The streamfunction, ψ, and velocity potential, ϕ, satisfy the Poisson equations

$$\nabla^2 \psi = \zeta, \qquad \nabla^2 \phi = \delta, \tag{F1}$$

from which the rotational and divergent velocity components were recovered as

$$u'_{\psi} = -\frac{\partial \psi}{\partial y}, \quad v'_{\psi} = \frac{\partial \psi}{\partial x}, \qquad \text{and} \qquad u'_{\phi} = \frac{\partial \phi}{\partial x}, \quad v'_{\phi} = \frac{\partial \phi}{\partial y}. \tag{F2}$$

We solved Equation F1 using a spectral method, which assumes a periodic domain. Because the finite gridded velocity field is not periodic, solving directly on the prediction grid introduced spurious short-wavelength energy into ψ and ϕ from the domain edges. To reduce this, at each time step the gridded ζ and δ fields were zero-padded by 10 grid cells on all four sides prior to solving. Taking ζ as an example, the padded field was Fourier transformed and Equation F1 solved in wavenumber space as

$$\hat{\psi}(\mathbf{k}) = -\frac{\hat{\zeta}(\mathbf{k})}{|\mathbf{k}|^2}, \qquad \mathbf{k} \neq 0, \tag{F3}$$

where $\mathbf{k} = (k_x, k_y)$ is the horizontal wavenumber vector. ϕ was obtained the same way, substituting δ for ζ in Equation F3. ψ and ϕ were recovered by inverse Fourier transform and the padding removed, returning both fields on the original grid, before computing $\mathbf{u'}_{\psi}$ and $\mathbf{u'}_{\phi}$ (Equation F2) and their respective horizontal kinetic energy.

https://doi.org/10.5194/egusphere-2026-6450
Preprint. Discussion started: 3 November 2026
© Author(s) 2026. CC BY 4.0 License.

Author contributions. All authors contributed equally to the conceptualisation, investigation, and methodology. W. Edge led the formal analysis and writing components. M. Rayson and N. Jones led the funding acquisition and project management.

Competing interests. Matt Rayson is an editor for EGU Ocean Science.

Acknowledgements. This work was funded by a research grant from Shell Australia Pty. Ltd. The authors thank Phil Watson for his work to secure and manage the funding through his position as Shell Chair at the University of Western Australia. The authors also thank Michael Bertolacci for sharing his notes on Vecchia's approximation. The authors acknowledge the use of Kaya, the High-Performance Computing facility at The University of Western Australia, and the technical assistance provided by the IT HPC team (https://doi.org/10.26182/dh5s-v482). Generative AI tools were used to document and check Python code.

https://doi.org/10.5194/egusphere-2026-6450
Preprint. Discussion started: 3 November 2026
© Author(s) 2026. CC BY 4.0 License.

References

Aravind, H., Özgökmen, T. M., and Allshouse, M. R.: Lagrangian analysis of submesoscale flows from sparse data using Gaussian Process Regression for field reconstruction, Ocean Modelling, 193, 102 458, https://doi.org/10.1016/j.ocemod.2024.102458, 2025.

Arbic, B. K., Müller, M., Richman, J. G., Shriver, J. F., Morten, A. J., Scott, R. B., Sérazin, G., and Penduff, T.: Geostrophic Turbulence in the Frequency–Wavenumber Domain: Eddy-Driven Low-Frequency Variability*, Journal of Physical Oceanography, 44, 2050–2069, https://doi.org/10.1175/JPO-D-13-054.1, 2014.

Astfalck, L.: Closed-form Covariance Functions in Space and Time from B-spline Spectral Densities, https://doi.org/10.48550/arXiv.2506.21953, 2026.

Balwada, D., LaCasce, J. H., and Speer, K. G.: Scale-dependent distribution of kinetic energy from surface drifters in the Gulf of Mexico, Geophysical Research Letters, 43, https://doi.org/10.1002/2016GL069405, 2016.

Berlinghieri, R., Trippe, B. L., Burt, D. R., Giordano, R. J., Srinivasan, K., Özgökmen, T., Xia, J., and Broderick, T.: Gaussian processes at the Helm(holtz): A more fluid model for ocean currents, in: Proceedings of the 40th International Conference on Machine Learning, edited by Krause, A., Brunskill, E., Cho, K., Engelhardt, B., Sabato, S., and Scarlett, J., vol. 202 of *Proceedings of Machine Learning Research*, pp. 2113–2163, PMLR, https://proceedings.mlr.press/v202/berlinghieri23a.html, 2023.

Bühler, O., Callies, J., and Ferrari, R.: Wave–vortex decomposition of one-dimensional ship-track data, Journal of Fluid Mechanics, 756, 1007–1026, https://doi.org/10.1017/jfm.2014.488, 2014.

Callies, J., Barkan, R., and Garabato, A. N.: Time Scales of Submesoscale Flow Inferred from a Mooring Array, Journal of Physical Oceanography, 50, 1065–1086, https://doi.org/10.1175/JPO-D-19-0254.1, 2020.

Caspar-Cohen, Z., Ponte, A., Lahaye, N., Carton, X., Yu, X., and Gentil, S. L.: Characterization of Internal Tide Incoherence: Eulerian versus Lagrangian Perspectives, Journal of Physical Oceanography, 52, 1245–1259, https://doi.org/10.1175/JPO-D-21-0088.1, 2022.

Chamberlain, M. A., Oke, P. R., Fiedler, R. A. S., Beggs, H. M., Brassington, G. B., and Divakaran, P.: Next generation of Bluelink ocean reanalysis with multiscale data assimilation: BRAN2020, Earth System Science Data, 13, 5663–5688, https://doi.org/10.5194/essd-13-5663-2021, 2021.

Chelton, D. B., Schlax, M. G., and Samelson, R. M.: Global observations of nonlinear mesoscale eddies, Progress in Oceanography, 91, 167–216, https://doi.org/10.1016/j.pocean.2011.01.002, 2011.

Chiswell, S. M., Rickard, G. J., and Bowen, M. M.: Eulerian and Lagrangian eddy statistics of the Tasman Sea and southwest Pacific Ocean, Journal of Geophysical Research: Oceans, 112, 2007JC004 110, https://doi.org/10.1029/2007JC004110, 2007.

Cressie, N.: Fitting variogram models by weighted least squares, Mathematical Geology, 17, 563–586, https://doi.org/https://doi.org/10.1007/BF01032109, 1985.

Elipot, S., Lumpkin, R., Perez, R. C., Lilly, J. M., Early, J. J., and Sykulski, A. M.: A global surface drifter data set at hourly resolution, Journal of Geophysical Research: Oceans, 121, 2937–2966, https://doi.org/10.1002/2016JC011716, 2016.

Ferrari, R. and Wunsch, C.: Ocean Circulation Kinetic Energy: Reservoirs, Sources, and Sinks, Annual Review of Fluid Mechanics, 41, 253–282, https://doi.org/10.1146/annurev.fluid.40.111406.102139, 2009.

Foreman-Mackey, D., Hogg, D. W., Lang, D., and Goodman, J.: emcee : The MCMC Hammer, Publications of the Astronomical Society of the Pacific, 125, 306–312, https://doi.org/10.1086/670067, 2013.

Gelman, A. and Rubin, D. B.: Inference from Iterative Simulation Using Multiple Sequences, Statistical Science, 7, https://doi.org/10.1214/ss/1177011136, 1992.

https://doi.org/10.5194/egusphere-2026-6450
Preprint. Discussion started: 3 November 2026
© Author(s) 2026. CC BY 4.0 License.

Gong, Y., Rayson, M. D., Jones, N. L., and Ivey, G. N.: Directional decomposition of internal tides propagating from multiple generation sites, Ocean Modelling, 162, 101 801, https://doi.org/10.1016/j.ocemod.2021.101801, 2021.

Goodman, J. and Weare, J.: Ensemble samplers with affine invariance, Communications in Applied Mathematics and Computational Science, 5, 65–80, https://doi.org/10.2140/camcos.2010.5.65, 2010.

Gordon, A. L.: Interocean exchange of thermocline water, Journal of Geophysical Research: Oceans, 91, 5037–5046, https://doi.org/10.1029/JC091iC04p05037, 1986.

Goring, D. G. and Nikora, V. I.: Despiking Acoustic Doppler Velocimeter Data, Journal of Hydraulic Engineering, 128, 117–126, https://doi.org/10.1061/(ASCE)0733-9429(2002)128:1(117), 2002.

Gray, A. R. and Riser, S. C.: A method for multiscale optimal analysis with application to Argo data, Journal of Geophysical Research: Oceans, 120, 4340–4356, https://doi.org/10.1002/2014JC010208, 2015.

Guinness, J.: Permutation and Grouping Methods for Sharpening Gaussian Process Approximations, Technometrics, 60, 415–429, https://doi.org/10.1080/00401706.2018.1437476, 2018.

Guyon, X.: Parameter estimation for a stationary process on a d-dimensional lattice, Biometrika, 69, 95–105, https://doi.org/10.1093/biomet/69.1.95, 1982.

Katzfuss, M. and Guinness, J.: A General Framework for Vecchia Approximations of Gaussian Processes, Statistical Science, 36, https://doi.org/10.1214/19-STS755, 2021.

Le Traon, P. Y.: A method for optimal analysis of fields with spatially variable mean, Journal of Geophysical Research: Oceans, 95, 13 543–13 547, https://doi.org/10.1029/JC095iC08p13543, 1990.

Middleton, J. F. and Garrett, C.: A kinematic analysis of polarized eddy fields using drifter data, Journal of Geophysical Research: Oceans, 91, 5094–5102, https://doi.org/10.1029/JC091iC04p05094, 1986.

Moss, H., Astfalck, L., Cowperthwaite, T., Doumont, C., Willis, S., Hennig, P., Nemeth, C., and Zammit-Mangion, A.: Conditioning Gaussian Processes on Almost Anything, arXiv preprint arXiv:2605.21041, https://doi.org/10.48550/arXiv.2605.21041, 2026.

Pattiaratchi, C.: Surface current data from ocean drifters in the Indian Ocean, https://doi.org/10.26198/e8j3-9533, 2025.

Pearson, J., Fox-Kemper, B., Pearson, B., Chang, H., Haus, B. K., Horstmann, J., Huntley, H. S., Kirwan, A. D., Lund, B., and Poje, A.: Biases in Structure Functions from Observations of Submesoscale Flows, Journal of Geophysical Research: Oceans, 125, e2019JC015 769, https://doi.org/10.1029/2019JC015769, 2020.

Ponte, A. L. S., Astfalck, L. C., Rayson, M. D., Zulberti, A. P., and Jones, N. L.: Inferring flow energy, space scales, and timescales: freely drifting vs. fixed-point observations, Nonlinear Processes in Geophysics, 31, 571–586, https://doi.org/10.5194/npg-31-571-2024, 2024.

Qiu, B., Chen, S., Klein, P., Wang, J., Torres, H., Fu, L.-L., and Menemenlis, D.: Seasonality in Transition Scale from Balanced to Unbalanced Motions in the World Ocean, Journal of Physical Oceanography, 48, 591–605, https://doi.org/10.1175/JPO-D-17-0169.1, 2018.

Rasmussen, C. E. and Williams, C. K. I.: Gaussian Processes for Machine Learning, The MIT Press, https://doi.org/10.7551/mitpress/3206.001.0001, 2006.

Rayson, M. D., Ivey, G. N., Jones, N. L., Meuleners, M. J., and Wake, G. W.: Internal tide dynamics in a topographically complex region: Browse Basin, Australian North West Shelf, Journal of Geophysical Research, 116, C01 016, https://doi.org/10.1029/2009JC005881, 2011.

Rayson, M. D., Astfalck, L. C., Ponte, A. L., Zulberti, A. P., and Jones, N. L.: Characteristic Velocity and Timescales of Nonphase-Locked Internal Tides in a Mesoscale Eddy Field, Journal of Geophysical Research: Oceans, 130, e2024JC021 789, https://doi.org/10.1029/2024JC021789, 2025.

https://doi.org/10.5194/egusphere-2026-6450
Preprint. Discussion started: 3 November 2026
© Author(s) 2026. CC BY 4.0 License.

Ridgway, K. R. and Godfrey, J. S.: The source of the Leeuwin Current seasonality, Journal of Geophysical Research: Oceans, 120, 6843–6864, https://doi.org/10.1002/2015JC011049, 2015.

Rio, M.-H., Mulet, S., and Picot, N.: Beyond GOCE for the ocean circulation estimate: Synergetic use of altimetry, gravimetry, and in situ data provides new insight into geostrophic and Ekman currents, Geophysical Research Letters, 41, 8918–8925, https://doi.org/https://doi.org/10.1002/2014GL061773, 2014.

Scharffenberg, M. G. and Stammer, D.: Statistical parameters of the geostrophic ocean flow field estimated from the Jason-1–TOPEX/Poseidon tandem mission, Journal of Geophysical Research, 116, C12 011, https://doi.org/10.1029/2011JC007376, 2011.

Siji, P. and Pattiaratchi, C.: Surface Current Observations in the Southeastern Tropical Indian Ocean Using Drifters, Journal of Marine Science and Engineering, 13, 717, https://doi.org/10.3390/jmse13040717, 2025.

Stammer, D.: On Eddy Characteristics, Eddy Transports, and Mean Flow Properties, Journal of Physical Oceanography, 28, 727–739, https://doi.org/10.1175/1520-0485(1998)028<0727:OECETA>2.0.CO;2, 1998.

Torres, H. S., Klein, P., Menemenlis, D., Qiu, B., Su, Z., Wang, J., Chen, S., and Fu, L.: Partitioning Ocean Motions Into Balanced Motions and Internal Gravity Waves: A Modeling Study in Anticipation of Future Space Missions, Journal of Geophysical Research: Oceans, 123, 8084–8105, https://doi.org/10.1029/2018JC014438, 2018.

Ubelmann, C., Dibarboure, G., Gaultier, L., Ponte, A., Ardhuin, F., Ballarotta, M., and Faugère, Y.: Reconstructing Ocean Surface Current Combining Altimetry and Future Spaceborne Doppler Data, Journal of Geophysical Research: Oceans, 126, e2020JC016 560, https://doi.org/10.1029/2020JC016560, 2021.

Ubelmann, C., Carrere, L., Durand, C., Dibarboure, G., Faugère, Y., Ballarotta, M., Briol, F., and Lyard, F.: Simultaneous estimation of ocean mesoscale and coherent internal tide sea surface height signatures from the global altimetry record, Ocean Science, 18, 469–481, https://doi.org/10.5194/os-18-469-2022, 2022.

van der Mheen, M., Pattiaratchi, C., Cosoli, S., and Wandres, M.: Depth-Dependent Correction for Wind-Driven Drift Current in Particle Tracking Applications, Frontiers in Marine Science, 7, 305, https://doi.org/10.3389/fmars.2020.00305, 2020.

Vecchia, A. V.: Estimation and Model Identification for Continuous Spatial Processes, Journal of the Royal Statistical Society. Series B (Methodological), 50, 297–312, https://doi.org/10.1111/j.2517-6161.1988.tb01729.x, 1988.

Wang, H.: Anisotropic Statistics of Lagrangian Structure Functions and Helmholtz Decomposition, Journal of Physical Oceanography, 51, https://doi.org/10.1175/JPO-D-20-0199.1, 2021.

Wortham, C. and Wunsch, C.: A Multidimensional Spectral Description of Ocean Variability, Journal of Physical Oceanography, 44, 944–966, https://doi.org/10.1175/JPO-D-13-0113.1, 2014.

Wunsch, C.: The Ocean Circulation Inverse Problem, Cambridge University Press, ISBN 9780511629570, https://doi.org/10.1017/CBO9780511629570, 1996.

Wunsch, C.: Modern Observational Physical Oceanography: Understanding the Global Ocean, Princeton University Press, Princeton, NJ, ISBN 9780691158822, 2015.

Wunsch, C. and Stammer, D.: The global frequency-wavenumber spectrum of oceanic variability estimated from TOPEX/POSEIDON altimetric measurements, Journal of Geophysical Research: Oceans, 100, 24 895–24 910, https://doi.org/10.1029/95JC01783, 1995.

Xia, J., Iskandarani, M., Gonçalves, R. C., and Özgökmen, T.: Error Quantification of Gaussian Process Regression for Extracting Eulerian Velocity Fields from Ocean Drifters, Journal of Marine Science and Engineering, 13, 431, https://doi.org/10.3390/jmse13030431, 2025.

Zang, X. and Wunsch, C.: Spectral Description of Low-Frequency Oceanic Variability, Journal of Physical Oceanography, 31, 3073–3095, https://doi.org/10.1175/1520-0485(2001)031<3073:SDOLFO>2.0.CO;2, 2001.

https://doi.org/10.5194/egusphere-2026-6450
Preprint. Discussion started: 3 November 2026
© Author(s) 2026. CC BY 4.0 License.



Zheng, Y., Rayson, M. D., Jones, N. L., and Astfalck, L. C.: A machine learning parameterization for the internal gravity wave spectrum, Journal of Geophysical Research: Oceans, 131, e2025JC023 028, https://doi.org/10.1029/2025JC023028, 2026.